

Unclassified

SECURITY CLASSIFICATION OF THIS PAGE (If different from block 1 Entered)

1 AB
3

11 REPORT DOCUMENTATION PAGE		READ INSTRUCTIONS BEFORE COMPLETING THIS FORM	3. RECIPIENT'S CATALOG NUMBER
1. REPORT NUMBER	2. GOVT ACCESSION NO.	S. TYPE OF REPORT & PERIOD COVERED	
AFOSR-TR-75-1079		Final (6/1/74 - 6/30/75)	
4. TITLE (and Subtitle)		6. PERFORMING ORG. REPORT NUMBER	
A Two Dimensional Global Climatic Model,		7. CONTRACT OR GRANT NUMBER(S)	
AUTHOR(s)		AFOSR-2633-74, VAPAR Order-2592	
10 William D. Sellers		10. PROGRAM ELEMENT, PROJECT, TASK AREA & WORK UNIT NUMBERS	
PERFORMING ORGANIZATION NAME AND ADDRESS		AO 2592 64706E	
University of Arizona Tucson, Ariz. 85721		12. REPORT DATE 7/2/75	
CONTROLLING OFFICE NAME AND ADDRESS		13. NUMBER OF PAGES 56	
Advanced Research Projects Agency/IPT 1400 Wilson Boulevard Arlington, VA 22209		14. SECURITY CLASS. (of this report) UNCLASSIFIED	
MONITORING AGENCY NAME & ADDRESS (if different from Controlling Office)		15a. DECLASSIFICATION/DOWNGRADING SCHEDULE	
Air Force Office of Scientific Research/NP 1400 Wilson Boulevard Arlington, VA 22209		17. DISTRIBUTION STATEMENT (of the abstract entered in Block 20, if different from Report) Final technical rpt. 1 Jan 74-30 Jun 75	
DISTRIBUTION STATEMENT (of this Report)		DDC REFINED JAN 15 1976 REGULATED D	
Approved for public release; distribution unlimited		18. SUPPLEMENTARY NOTES	
		19. KEY WORDS (Continue on reverse side if necessary and identify by block number) Climate Modeling Climate Change	
20. ABSTRACT (Continue on reverse side if necessary and identify by block number)		A two-dimensional global climatic model has been developed, using a 10° longitude by 10° latitude box grid and a one-month time step. The lapse rates of temperature and the meridional component of the flow in the oceans and atmosphere and of specific humidity in the atmosphere are parameterized in terms of their respective sea-level values. The model then utilizes (cont on p1473 b) ←	

unclassified

SECURITY CLASSIFICATION OF THIS PAGE(When Data Entered)

20. Abstract (continued)

(cont'd p 1473A)

the vertically-averaged thermodynamic energy equation, the equation of motion for the boundary layer, the thermal wind equation, the hydrostatic equation, the surface water balance equation, and empirical relations between the sea-level temperature and pressure gradient fields and between cloud cover and precipitation to determine the global distribution by months of sea-level pressure, temperature, wind speed and direction, and relative humidity, precipitation, evaporation, runoff, soil moisture content, ice and snow cover and thickness, cloud cover, and poleward energy transport. A simple ocean model is included.

Two 100 model-year runs were made on the NCAR CDC 7600 computer. Each required about 27 minutes of computer time. They differed only in the value of the solar constant used. Both runs indicate that the model is extremely stable. In almost all grid boxes only minor changes in any variable in any month occurred after the first 40 to 50 years. There are strong similarities between computed and observed fields of many of the variables. However, there are also several cases where the model predictions are completely unrealistic.

ACCESSION for	
NTIS	White Section <input checked="" type="checkbox"/>
BBC	Buff Section <input type="checkbox"/>
UNANNOUNCED	<input type="checkbox"/>
JUSTIFICATION.....	
.....	
BY.....	
DISTRIBUTION/AVAILABILITY CODES	
Dist.	AVAIL. and/or SPECIAL
A	

AFOSR - 75 - 1079

Form Approved
Budget Bureau No. 22-R0293

A Two Dimensional Global Climatic Model

Final Technical Report for the Period 6/1/74 to 6/30/75

AD-A0-145824

Sponsored by

Advanced Research Projects Agency

ARPA Order No. 2592

Principal Investigator - William D. Sellers (1-602-884-1352)

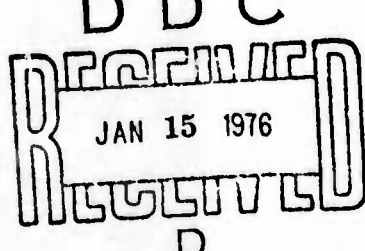
Contractor - Air Force Office of Scientific Research

Contract No. - AFOSR-74-2633

AIR FORCE OFFICE OF SCIENTIFIC RESEARCH (AFSC)
NOTICE OF TRANSMITTAL TO DDC
This technical report has been reviewed and is
approved for public release IAW AFR 190-12 (b).
Distribution is unlimited.

D. W. TAYLOR
Technical Information Officer

Program Code 4P10
Effective Date of Contract - 11/15/73
Contract Expiration Date - 6/30/75 (extended)
Amount of Contract - \$30,666



July 2, 1975

A Two-Dimensional Global Climatic Model

1. Summary

In recent articles (Sellers, 1973, 1974) the author describes a simple global climatic model applied to an earth with one large ocean and one large continent, extending with variable width from pole to pole. The model might be classified as a $1\frac{1}{2}$ -dimensional model in that the zonal, east-west, resolution is limited to differentiation only between one temperature for the ocean surface and one temperature for the land surface within each 10° latitude band. The purpose of this paper is to discuss an extension of the model to a box grid, each box having dimensions of 10° of latitude and longitude, thus permitting better zonal resolution but increasing the required computer time by a factor of about 200.

The basic concepts used with the earlier model have been applied to the two-dimensional box model with only a few pertinent changes introduced in order to reduce the number of arbitrary constants used. Included is the incorporation of a complete hydrologic cycle. The major assumptions used are the following:

- a. Air temperature T decreases linearly with increasing height at a rate equal to 6.5 K km^{-1} ;
- b. Vapor pressure e decreases with increasing height at a rate equal to $34(1 + a_1)eT^{-1} \text{ hPa km}^{-1}$, where a_1 is a specified function of the sea-level vapor pressure, which in turn depends on the sea-level temperature and relative humidity.

- c. The meridional velocity component v varies linearly with pressure p , ranging from v_o at $p = p_o = 1000 \text{ hPa}$ to 0 at $p = 600 \text{ hPa}$ to $-v_o$ at $p = p_2 = 200 \text{ hPa}$.
- d. The meridional sea-level pressure gradient averaged over all longitudes is proportional to the corresponding sea-level temperature gradient, with the constant of proportionality itself inversely proportional to the zonally-averaged surface friction coefficient.
- e. Water temperature T_w of the oceans decreases exponentially with depth, approaching at great depths 274 K or the average surface temperature at 65 S, whichever is higher.
- f. The north-south wind-driven current component v_w also varies exponentially with depth, going to zero and changing sign at a depth which depends on the vertical eddy diffusivity.
- g. The solar radiation absorbed by an earth-atmosphere column and the infrared radiation emitted to space are known functions of the atmospheric composition (given, except for the water vapor content), cloud cover, and the surface temperature and albedo (which depends partly on the snow and ice cover).

To determine the sea-level temperature and pressure fields from a vertically integrated version of the thermodynamic energy equation for the earth-atmosphere system, these assumptions are coupled with appropriate forms of the equations of motion for the boundary layer (to determine the surface wind components), the

thermal wind equation (to determine the variation with height of the zonal wind component), and Ekman's equations for wind-driven ocean currents (to relate the surface current to the surface wind).

The components of the hydrologic cycle are determined from the water budgets for the surface and the atmosphere. This is done using estimates of the storage rate of water vapor in the atmosphere and the divergence of the water vapor flux by the atmospheric circulation to obtain the difference between monthly evaporation and precipitation rates for each grid box. Over the oceans the evaporation rate may be estimated from established formulae relating it to the near-surface wind speed, temperature, and relative humidity. Over land evaporation rates depend mainly on the amount of water in the soil and the potential evapotranspiration rate and may be determined from the water balance equation for a soil column using a simple bookkeeping approach. As by-products here, the soil moisture content and runoff rates are obtained.

Knowing the evaporation rate, the monthly precipitation may be determined directly (with the necessary constraint that it may never be less than zero). Depending on the surface temperature, a prescribed fraction of this precipitation will fall as snow, adding to that which may be already present on the ground or ice. Sea ice forms if the air temperature is at or below freezing and decreasing. It melts from below when the temperature

is rising. Both snow and ice may melt at the surface when the temperature is above freezing. Part of the snow melt over land can infiltrate into the soil, increasing the soil moisture content. The fraction of each box covered by snow and/or ice is a simple function of their respective depths.

The relative humidity over water, snow, or ice may be expressed as the mid-ocean value (prescribed as a function of latitude) modified by the zonal advection of wetter or drier air from upwind regions. Over land the surface relative humidity depends on the soil moisture content. To complete the cycle, cloud cover is empirically estimated from the precipitation and evaporation rates and the surface relative humidity.

With the incorporation of a hydrologic cycle, the only prescribed variables in the model (other than the mid-ocean relative humidity) are the extraterrestrial solar radiation and the amounts of CO₂ and O₃ in the atmosphere. Everything else can vary. With such a system, incorporating numerous feedbacks, both positive and negative, it is possible that, without proper coupling, one process may dominate and, after a sufficiently long run of the model, produce nonsense results. Therefore, a couple of runs of 100 model years were made on the NCAR CDC 7600 computer to check the stability of the model. The results of this analysis will be discussed in section 3 of this paper. Also discussed is an analysis of the stability of the ice packs of the Arctic and Antarctic.

2. Model structure

The model assumes an atmosphere (troposphere) with constant lapse rate (6.5 K km^{-1}) extending from sea level, with pressure p_0 , to $p_2 = 200 \text{ hPa}$. Thus,

$$T = T_0 \left(\frac{p}{p_0} \right)^{0.19}, \quad (1)$$

where T_0 is the sea-level temperature. It then follows from the hydrostatic equation and the thermal wind equation that

$$h = \frac{R_d}{0.19g} (T_0 - T) \quad (2)$$

and

$$u = u_0 - \frac{gh}{fT_0} \frac{\partial T_0}{\partial y}, \quad (3)$$

where R_d is the gas constant for dry air ($287.04 \text{ J kg}^{-1} \text{ K}^{-1}$), g is gravity (980 cm sec^{-2}), h is height above sea level, f is the coriolis parameter, and u is the zonal wind speed.

It is also assumed that

$$e = e_0 \left(\frac{p}{p_0} \right)^{1+a}, \quad (4)$$

and

$$v = v_0 \left(\frac{2p - p_0 - p_2}{p_0 - p_2} \right), \quad (5)$$

where e is the vapor pressure and v is the meridional wind speed.

As in Sellers (1973),

$$1 + a_1 = \frac{0.635e_o}{0.213 + 0.152e_o} , \quad (6)$$

where e_o is the surface vapor pressure (hPa) obtained from the Clausius-Clapeyron equation and from values of the surface relative humidity estimated from the hydrologic cycle component of the model.

The surface velocity components u_o and v_o within the friction layer are obtained from the equations of motion in the form

$$fv_o - a_2 |u_o| u_o - \frac{R_d T_o}{p_o} \frac{\partial p_o}{\partial x} = 0 \quad (7)$$

$$fu_o + a_2 |v_o| v_o + \frac{R_d T_o}{p_o} \frac{\partial p_o}{\partial y} = 0 , \quad (8)$$

where the surface friction coefficient a_2 equals $4 \times 10^{-7} \text{ cm}^{-1}$ for land and ice and $2 \times 10^{-8} \text{ cm}^{-1}$ for water. By differentiating (1) with respect to x , assuming that

$$\frac{\partial p}{\partial x} = \rho f v , \quad (9)$$

where ρ is the air density, and integrating from p_0 to p_2 , it follows that

$$\frac{\partial p_0}{\partial x} = -0.613 \frac{p_0}{T_0} \frac{\partial T_0}{\partial x} . \quad (10)$$

The sea-level pressure field can be determined uniquely from (10) if, in addition, the pressure at one pole and the meridional pressure gradient averaged over all longitudes are known. There does not seem to be any analytic way to determine the latter. Therefore, it is arbitrarily expressed as a function of the corresponding averaged sea-level temperature gradient.

That is,

$$\frac{\partial \bar{p}_0}{\partial y} = \frac{b}{a} \frac{\partial \bar{T}_0}{\partial y} , \quad (11)$$

where the bars represent zonal means. The values of b used are given in Table 1. The inclusion of the averaged surface friction coefficient in (11) permits asymmetry in the wind field between the two hemispheres, with the strongest surface westerlies in mid-latitudes of the southern hemisphere.

For the oceans, it is assumed that

$$T_w = T_{WB} + (T_o - T_{WB}) e^{-az} \quad (12)$$

and

$$v_w = v_{wo} e^{-az} (1 - az) , \quad (13)$$

where T_{WB} is the (given) temperature of the bottom water, taken to equal 274 K or the average annual surface temperature at 65 S, whichever is higher (see Dietrich, 1963, p. 184). v_w should be interpreted here as the meridional component of the component of the current at depth z in the direction of the net mass transport. From the classical theory of heat transfer in a homogeneous medium, the exponent a should equal $(\pi/P\kappa)^{1/2}$, where P is the period of the oscillation (12 months in this case) and κ is the vertical eddy diffusivity. From Ekman's theory for pure drift currents in a homogeneous ocean (Neumann and Pierson, 1966, p. 192), the depth D of the layer of frictional influence should approximately equal π/a . With $\kappa = 1.5 \text{ cm}^2 \text{ sec}^{-1}$ (Haney, 1974), $D = 122\text{m}$.

Table 1. The b coefficients in (11) and the mid-ocean relative humidities RH_w used in the model

latitude	$b (10^7 \text{ hPa cm}^{-1}\text{K}^{-1})$	latitude belt	RH_w (percent)
80N	-1.9	80-90N	88
70	-0.5	70-80	87
60	1.0	60-70	85
50	0.9	50-60	82
40	0.2	40-50	78
30	-0.6	30-40	78
20	-1.6	20-30	80
10	-2.0	10-20	84
0	0	0-10	86
10	-2.0	0-10	86
20	-1.6	10-20	84
30	-0.6	20-30	80
40	0.2	30-40	78
50	0.4	40-50	78
60	1.0	50-60	82
70	-0.5	60-70	85
80S	-1.9	70-80	87
		80-90S	88

In (13) the meridional circulation v_w reverses direction at a depth equal to a^{-1} , or 39m if $\kappa = 1.5 \text{ cm}^2 \text{ sec}^{-1}$, which seems to be in reasonable agreement with observations (see, for example, Neumann and Pierson, 1966, p. 446). For ocean depths greater than about 500m, (13) integrated vertically yields essentially no net poleward mass transfer of water.

The surface current is assumed to result from the drag of the wind passing over homogeneous water. In this case Ekman's classical theory gives for the meridional component v_{wo} of the component of the surface wind-driven current in the direction of the net mass transport

$$v_{wo} = \mp C_1 u_o , \quad (14)$$

where the minus sign applies to the northern hemisphere and the positive sign to the southern hemisphere. v_{wo} is directed 90° to the right of the zonal wind in the northern hemisphere and 90° to the left of the zonal wind in the southern hemisphere. Following Thorade,

$$C_1 = 0.0001522(|f|)^{-\frac{1}{2}} \text{ when } |v| = (u_o^2 + v_o^2)^{\frac{1}{2}} \geq 600 \text{ cm sec}^{-1}$$

and

$$C_1 = 0.003728(|fv|)^{-\frac{1}{2}} \text{ when } |v| < 600 \text{ cm sec}^{-1} .$$

The constant in the latter expression for C_1 is not equivalent to that given by Thorade, but is used here so that both expressions will give the same value for C_1 when $|v| = 600 \text{ cm sec}^{-1}$. (See Neumann and Pierson, 1966, pp. 192, 210, and Adem, 1970, pp. 415, 416.) Initial runs of the model with this formulation indicate instabilities arising near the equator because of the small values of the coriolis parameter f there. To get around this, it is assumed that $f = 10^{-4} \text{ sec}^{-1}$ at all latitudes.

With the above assumptions all the variables, T , T_w , h , u , v , v_w , and e , in the problem can be expressed as functions of the sea-level temperature T_0 and the air pressure p . They are related to one another through the thermodynamic energy equation integrated vertically through the earth-troposphere system.

$$R = \frac{1}{g} \int_{p_2}^{p_0} \overline{\frac{d}{dt}(Lq + c_p T + gh)} dp + C \int_0^d \overline{\frac{dT}{dt}} E dz , \quad (15)$$

where the bar represents a time (one month) average. R is the net available radiation for a column extending from p_2 to that depth d in the soil or water where the vertical flux of energy is negligible; L is the latent heat of condensation (2470 J gm^{-1}); c_p is the specific heat of air at constant pressure ($1005 \text{ J kg}^{-1}\text{K}^{-1}$); C is the heat capacity of soil or water; and T_E is the average temperature of the soil or water column.

Each of the total derivatives on the right-hand side of (15) may be expanded in the approximate form

$$\frac{ds}{dt} = \frac{\partial \bar{s}}{\partial t} + \frac{\partial}{\partial x} \bar{u} \bar{s} + \frac{\partial}{\partial y} (\bar{v} \bar{s} - K_S \frac{\partial \bar{s}}{\partial y}) + \frac{\partial}{\partial p} \bar{w} \bar{s}, \quad (16)$$

where $\omega = dp/dt$; s is either Lq , $c_p T$, gh , or CT_E ; and K_S is the eddy diffusivity for either latent heat ($S = V$), sensible heat ($S = H$ in the atmosphere; $S = F$ in the oceans), or potential energy ($S = P$). The term involving the eddy diffusivity represents a parameterization of the combined effects of the standing and transient eddies of the general circulation of the atmosphere or oceans.

Introducing (16) into (15) and using (1) - (5), (12), and (13) gives

$$\begin{aligned} gR/p_o &= c_p [a_{GH} \frac{\partial T_o}{\partial t} + a_{xH} u_o \frac{\partial T_o}{\partial x} + \frac{\partial}{\partial y} (a_{MH} v_o T_o - a_{EH} K_H \frac{\partial T_o}{\partial y})] \\ &\quad + R_d [a_{GP} \frac{\partial T_o}{\partial t} + a_{xP} u_o \frac{\partial T_o}{\partial x} + \frac{\partial}{\partial y} (a_{MP} v_o T_o)] \\ &\quad + L [a_{GV} \frac{\partial q_o}{\partial t} + a_{xV} u_o \frac{\partial q_o}{\partial x} + \frac{\partial}{\partial y} (a_{MV} v_o q_o - a_{EV} K_V \frac{\partial q_o}{\partial y})] \\ &\quad + C_w \frac{g}{p_o} [a_{GW} \frac{\partial T_o}{\partial t} + \frac{\partial}{\partial y} (a_{MW} v_{wo} T_o - a_{EW} K_W \frac{\partial T_o}{\partial y})] + C_L \frac{g}{p_o} a_{GL} \frac{\partial T_o}{\partial t} \end{aligned} \quad (17)$$

where $a_{GH} = a_{EH} = 0.717$, $a_{xH} = -0.371 \frac{R_d}{f u_o} \frac{\partial T_o}{\partial y} + 0.717$, $a_{MH} = 0.0331$

$$\begin{aligned}
 a_{GP} &= 0.439, \quad a_{XP} = -0.358 \frac{R_d}{fu_o} \frac{\partial T_o}{\partial y} + 0.439, \quad a_{MP} = -0.174 \\
 a_{GV} = a_{EV} &= \frac{1 - 0.2^{1+a_1}}{1 + a_1}, \quad a_{MV} = \frac{a_1 - 0.5 + (2.5 + a_1) 0.2^{1+a_1}}{(1 + a_1)(2 + a_1)}, \\
 a_{xV} &= \frac{R_d}{0.19 fu_o} \frac{\partial T_o}{\partial y} \left[\frac{1}{1.19 + a_1} (1 - 0.2^{1.19+a_1}) - \frac{1}{1 + a_1} (1 - 0.2^{1+a_1}) \right] \\
 &\quad + \frac{1}{1 + a_1} (1 - 0.2^{1+a_1}),
 \end{aligned}$$

$$a_{GW} = a_{EW} = a^{-1}, \quad a_{MW} = \frac{1}{4a} (1 - \frac{F_{WB}}{T_o}), \quad \text{and} \quad a_{GL} = (\rho K_L / \pi)^{\frac{1}{2}}$$

For a given grid box only one of the last two terms in (17) is used depending on whether the surface is water or land. Values of $0.167 \text{ J cm}^{-2} \text{ K}^{-1} \text{ sec}^{-\frac{1}{2}}$, $1.5 \text{ cm}^2 \text{ sec}^{-1}$, and $5 \times 10^8 \text{ cm}^2 \text{ sec}^{-1}$, respectively, are used for $C_L K_L^{\frac{1}{2}}$, κ , and K_W , the oceanic equivalent of K_H . As in Sellers (1973), it is assumed that

$$K_H = K_V = 0.25 |\Delta T_o| \times 10^{10} \text{ cm}^2 \text{ sec}^{-1}, \quad (18)$$

where ΔT_o is the surface temperature difference over 10° of latitude.

Because the model contains no stratosphere, the zonal wind increases without limit to the top of the atmosphere. This yields unrealistically large values for the divergences of the zonal transport of water vapor, heat, and potential energy.

To get around this, the magnitude of each divergence is constrained and not permitted to exceed about 160 Wm^{-2} . This is done by not allowing the magnitudes of $a_{xV}u_o$, $a_{xH}u_o$, and $a_{xP}u_o$ to exceed 20, $1.4A$, and $4.9A \text{ cm sec}^{-1}$, respectively, where A is the box area in units of 10^{14} cm^2 . The restriction on the magnitude of the zonal vapor flux divergence should be kept in mind, since it will have a slight influence on the precipitation field obtained.

The net radiation is determined as described earlier (Sellers, 1973, 1974). Snow and ice cover, cloud cover, and the sea-level relative humidity, all strongly influencing the radiation field, are obtained from the hydrologic cycle. To do this the first step is to estimate the difference between the rates of evaporation E and precipitation r from estimated or previously-determined values for the vapor flux divergence and the change in atmospheric moisture storage. This is done for each grid box. Over the oceans and snow-covered land the surface relative humidity RH of the j -th box is estimated from

$$RH = RH' = 0.5(RH_w + e'/e_s) , \quad (19)$$

where RH_w is the mid-ocean relative humidity (specified, see Table 1), e' is the surface vapor pressure of the upwind box at the same latitude and e_s is the saturation vapor pressure of the j -th box. The evaporation rate in cm mo^{-1} may then be determined from

$$E = E_{pt} = E' = 0.004|v|e_s(1 - RH) , \quad (20)$$

which is essentially the equation used by Budyko (1974).

Over snow-free land at temperatures above 271K the potential evapotranspiration rate E_p in cm mo^{-1} is given by

$$E_p = 0.0016(T_s - 271)^3, \quad (21)$$

where T_s is the surface temperature. This relationship was derived from data given by McIlroy and Angus (1964) for Aspendale, Australia. Actual evapotranspiration from land, which may be partially snow-covered, is estimated from

$$E = w_1 E_p (1 - A_s) / w_k + E' A_s, \quad (22)$$

where w_1 is the soil moisture content at the start of the given month, w_k is the critical soil moisture content, below which evaporation proceeds at less than the potential rate. It is assumed to equal 0.75 of the moisture content w_m at field capacity. A value of 24 cm is currently used in the model for w_m . A_s is the fraction of the box covered by snow. This is obtained from

$$A_s = 0.1 s_d \quad (s_d < 10 \text{ cm}) \quad (23)$$

where s_d is the existing value for the average snow depth in cm (water equivalent). In (22) when $w_1 > w_k$, the ratio of the two

is set equal to 1.0. Knowing the evaporation rate from (20) and/or (22) and the difference $E-r$, the precipitation rate may be obtained directly, with the condition that it cannot be less than zero.

In order to estimate cloud cover and the surface albedo, both needed in the radiation calculations, it is now necessary to redetermine the snow and ice coverage and the soil moisture content. To do this, it is first assumed that the snowfall s equals 0 when T_s is greater than 275K and equals r when T_s is less than 265K. In between

$$s = (27.5 - 0.1 T_s)r . \quad (24)$$

It is further assumed that the potential snow melt equals $7.5 E'$. The actual snow melt s_m , of course, cannot exceed the amount of snow present initially plus the snowfall. If s'_d is the average snow depth at the beginning of a given month, then its value at the end of the month is

$$s_d = s'_d + s - s_m A_s \quad \text{over land} \quad (25)$$

and

$$s_d = s'_d + (s - s_m (A_s)) A_i \quad \text{over water.} \quad (26)$$

An exception to (25) is made in Antarctica and Greenland. The

depths of these two ice caps are held constant.

A_i in (26) is the fraction of the box covered by ice. It is related to the existing value for the average ice thickness i_d in cm by

$$A_i = 0.003 i_d \quad (i_d < 333 \text{ cm}) \quad (27)$$

The ice thickness can change by melting i_m or freezing i_f from below or by melting i'_m from above in snow-free regions at a rate equal to or less than the potential rate $7.5E'$. It is assumed that

$$i_m = 6(T_s - T'_s) , \quad i_f = 0 \quad \text{when } T_s > T'_s \quad (28)$$

and

$$i_f = 6(T'_s - T_s) , \quad i_m = 0 \quad \text{when } T_s < T'_s < 275K , \quad (29)$$

where T'_s is the surface temperature at the start of the given month. The numerical value of the constant was selected on the basis of a statement made by Wittman and Schule (Fletcher, 1966, p. 219) to the effect that one season's growth of ice varies from 157 to 183 cm. In (28) i_m cannot exceed the total amount of ice that can be melted. The ice thickness i_d at the end of the month

is given by

$$i_d = i'_d + i_f - (i_m + i'_m - s_m A_s) A_i . \quad (30)$$

The heat required to melt the ice from below and that released by the formation of snow and ice are included in the energy conservation equation. The energy used to melt surface snow and ice is already included in the evaporation term.

With s_d and i_d obtained from (25) or (26) and (30), A_s and A_i may be redetermined from (23) and (27). The surface albedo α_s over water may then be estimated from

$$\alpha_s = (0.8 A_s + 0.6(1 - A_s)) A_i + (1 - A_i) \alpha_w , \quad (31)$$

where α_w is the albedo of open water (prescribed as a function of latitude and time of year) and values of 0.8 and 0.6, respectively, are used for the albedos of snow and ice.

Over land the surface albedo depends to some extent on the soil moisture content. This is estimated from the water balance for a soil column. Following Sellers (1965) and assuming that runoff r_o is given by

$$r_o = 0.8 \frac{\bar{w} r'^2}{\bar{w}_m (E_p' + r')} = b_1 \bar{w} \quad (32)$$

where r' is the effective precipitation,

$$r' = r + s_m \lambda_s - s \quad (33)$$

and that

$$E = E'_p = E_p (1 - A_s) \quad \text{when } \bar{w} \geq w_k \quad (34)$$

and

$$E = \bar{w} E'_p / w_k \quad \text{when } \bar{w} < w_k , \quad (35)$$

where $\bar{w} = 0.5(w_1 + w_2)$ is the average soil moisture content for the month, it follows that

$$\bar{w} = \frac{2w_1 - E'_p + r'}{2 + b_1} \quad \text{when } \bar{w} \geq w_k \quad (36)$$

$$\text{and } \bar{w} = \frac{2w_1 + r'}{2 + b_1 + E'_p / w_k} \quad \text{when } \bar{w} < w_k . \quad (37)$$

Note that (34) and (35) are different than (22). This is because the latter is only an estimate of total evaporation from land and is used to determine the precipitation rate. In (34) and (35) it is assumed that evaporation from the snow-covered portion of

the grid box does not affect the water budget of the soil column. Having determined \bar{w} and, hence w_2 , which becomes w_1 for the following month, the surface albedo for land is obtained from

$$\alpha_s = 0.8A_s + (1 - A_s)(0.3 - 0.25 \bar{w}/w_m) . \quad (38)$$

Further, the surface relative humidity and total potential evapotranspiration are given by

$$RH = 0.9(1 - A_s)\bar{w}/w_m + A_s RH' \quad (39)$$

and

$$E_{pt} = E'_p + A_s E' \quad (40)$$

To conclude the cycle, it is assumed that cloud cover n is related to the relative humidity and the precipitation and total potential evapotranspiration rates by

$$n = (0.75 + 0.25 \frac{r - E_{pt}}{r + E_{pt}})RH , \quad (41)$$

where the coefficients have been determined so as to give an average cloud cover of slightly greater than 0.5 under present conditions. In the model, then, cloud cover increases with

increasing precipitation, increasing relative humidity, and decreasing potential evapotranspiration (or decreasing temperature).

A simple flow diagram will be used to show the logic of the model. This is presented in Figure 1 and explained in the following paragraphs.

The first step is to estimate or specify the sea-level temperatures for each grid box at the beginning and middle of a given month (block 0). The calculations are started with January and the two temperatures are assumed equal. The sea-level pressure, wind, and ocean current fields corresponding to the specified temperature field are computed next for the whole grid (block 1). Using estimated relative humidities (either specified or those for the previous month), the sea-level vapor pressure is then determined for each box (block 2).

The calculations in the next three blocks are carried out at one longitude i at a time. First, the temperature and moisture dependent parameters are evaluated (block 3). These are principally the coefficients relating vertical integrals in the thermodynamic energy equation to their sea-level values. Next (block 4) the components of the hydrologic cycle, including cloud cover and surface albedo, are computed. This requires specified or predetermined estimates for ice and snow thickness and the soil moisture content, as outlined earlier. Then, in block 5, the sea-level temperature in each 10° latitude box

is determined from the energy equation.

When this cycle is completed for all longitudes, the resulting temperatures for each box are compared with those used originally (block 6). If each pair of temperatures differs by no more than a specified amount (which varies with latitude, ranging from 1.0K near the poles to 0.2K near the equator) the calculations proceed directly to block 7. Otherwise, the initial temperatures are adjusted and the sequence of blocks 2, 3, and 5 repeated (but never more than six times). Notice that the components of the hydrologic cycle are not recomputed here.

When the temperatures have converged or the above cycle has been completed six times, the temperatures at one longitude (arbitrarily, at 5°W) are compared with those used originally to find the pressure and wind fields (block 7). Whether they agree or disagree by a specified amount (1.0K), the program returns to block 1. With non-convergence, the complete cycle, including the calculation of the components of the hydrologic cycle, is repeated, but not more than ten times. Satisfactory convergence is usually achieved after no more than four cycles, in which case a final pass is made through block 5, with final values for snow and ice depths and the soil moisture content made along the way (block 8). After the values of desired variables are printed out (block 9) the program proceeds to the next month (block 0). At the end of each year of calculations

the average annual temperature in each box and the temperature of the bottom water of the oceans are recomputed.

3. Results

In order to test its stability two 100 year runs were made with the model, using solar constants, respectively, of 1353 and 1360 Wm^{-2} (1.94 and 1.95 ly min^{-1}). Each run required approximately 27 minutes of computer time on the NCAR CDC 7600.

Considering all the feedback loops involved, the model turned out to be surprisingly stable. Starting with realistic initial conditions, convergence was quite rapid with only minor changes occurring in any variable after the first 50 years. Even after 10 years most changes were quite small, the largest occurring in the Arctic Ocean north of Alaska, where sea ice had not yet reached its equilibrium value.

The stability of the model is illustrated in Table 2 and Figure 2. In the table are given for January and July hemispheric values of sea ice area and global average values of sea-level temperature, precipitation, and cloud cover at 10-year intervals for the two selected values of the solar constant. The time variation of the sea ice area (the average of the July and January values) is shown by the solid lines in Figure 2 for the northern (N and N1) and southern (S and S1) hemispheres, the higher values (N1 and S1) applying to the lower solar constant.

Sea ice area seems to be the most sensitive of the variables and the slowest to reach an equilibrium value. For the low solar constant case, even after 100 years, sea ice still is increasing very slowly in the northern hemisphere, especially in July. After 30 to 40 years there is no apparent trend in temperature, precipitation, or cloud cover. These variables appear to be especially stable for the higher solar constant case.

Estimates of the observed values of the variables in Table 2 are given in the last line of that table. The sea ice area values are estimated from data given by Vowinckel and Orwig (1970) and Gordon and Taylor (1975). Temperature (corrected to sea level) and precipitation values are from Schutz and Gates (1971, 1972), and cloud cover from Brooks (1927), modified near the poles by the author. The precipitation values are averages for Dec.-Feb. and June-Aug.

Allowing for a reasonable margin of error, the model and observed values agree fairly well. The largest discrepancies are in the sea ice area for the southern hemisphere. The model not only gives too much ice, by a factor of about two, but also does not reproduce the observed large seasonal variation in coverage. Yet the model does do quite well in the northern hemisphere in both months. These different results may possibly be related either to the significantly higher salinity and upwelling

in the Antarctic Ocean than in the Arctic Basin (Neumann and Pierson, 1966) or to the strong katabatic winds off the Antarctic continent. These winds, however, would be more likely to increase the ice area than to decrease it.

The model global average temperatures are in reasonable agreement with the observed values, especially in July. In January the model value is slightly too high, probably because the parameterization (1) does not permit the formation of surface inversions. As will be seen later, the departures from observed temperatures are largest in polar latitudes.

The model predicts greater precipitation in July than in January. The data of Schutz and Gates (1971, 1972) suggest the opposite. Not too much significance should probably be attached to this result, because of the great difficulty involved in determining average precipitation rates for large portions of the globe. The same must also be true of cloud cover, although here satellite data should eventually yield reliable observed values. Note that between months and between solar constant values there is an inverse relationship between precipitation and cloud cover, in spite of (41) which says that the two should increase and decrease together. The inverse relationship between cloud cover and potential evapotranspiration (or temperature) in (41) apparently dominates.

As an interesting sidelight of Table 2, a 0.5 percent decrease of the solar constant yields a 9.6 percent increase in sea ice area, a 1 K drop in temperature, an 8.4 percent decrease in precipitation, and a 1.1 percent increase in cloud cover.

Two 10-year runs were conducted to study the stability of the polar ice using a solar constant of 1360 Wm^{-2} . In both as an initial condition it was assumed that there was no ice or snow anywhere on the earth. In the first run, the results of which are shown by the dashed lines in Figure 2, initial temperatures used were those presently observed at the start of January. In the second run, the results of which are shown by the dash-dotted lines in the figure, these temperatures were adjusted within each box by multiplying by 0.4 and adding 183. Since the original temperatures ranged from 230 to 305K, the new values ranged from 275 to 305K, or everywhere above freezing. In both runs the sea ice reformed and after 10 years was a significant fraction of the equilibrium values, especially in the first run. It is interesting to note that in the second run the Antarctic sea ice was rather slow to get started and until the seventh year covered a smaller area than the Arctic ice. Both of these runs indicate that sea ice is a relatively stable feature of the model.

A more detailed comparison of observed and computed variables for January and July is shown in Figures 3 to 7. Again, a solar constant of 1360 Wm^{-2} is used. The observed data for temperature,

Table 2. Hemispheric values of the sea ice area (10^{16}cm^2) and global average values of sea-level temperature \bar{T}_o ($^{\circ}\text{C}$), precipitation $r(\text{cm mo}^{-1})$ and cloud cover \bar{n} in January and July at 10 year intervals with a solar constant of (a) 1353 Wm^{-2} and (b) 1360 Wm^{-2} .

Year	January						July					
	Sea Ice Area						Sea Ice Area					
	NH	SH	\bar{T}_o	\bar{r}	\bar{n}	NH	SH	\bar{T}_o	\bar{r}	\bar{n}		
(a)	10	12.1	21.2	14.2	6.1	0.533	9.4	23.3	16.0	7.6	0.520	
	20	12.4	22.1	14.0	5.9	0.535	9.6	23.9	15.9	7.5	0.522	
	30	12.7	22.4	13.9	5.9	0.534	9.9	24.0	15.8	7.4	0.523	
	40	12.9	22.4	13.8	5.8	0.534	10.0	24.0	15.7	7.3	0.525	
	50	12.9	22.4	13.8	5.8	0.535	10.1	24.0	15.7	7.3	0.524	
	60	13.0	22.3	13.8	5.8	0.535	10.2	23.9	15.7	7.4	0.525	
	70	13.0	22.3	13.8	5.8	0.535	10.3	23.9	15.7	7.3	0.525	
	80	13.0	22.3	13.8	5.8	0.535	10.3	23.9	15.7	7.3	0.525	
	90	13.0	22.2	13.8	5.8	0.535	10.3	23.9	15.7	7.3	0.525	
	100	13.0	22.2	13.8	5.8	0.535	10.4	23.9	15.7	7.3	0.525	
(b)	10	11.4	20.8	14.8	6.3	0.530	8.7	22.8	16.6	7.9	0.519	
	20	11.2	21.5	14.8	6.3	0.530	8.5	23.2	16.6	8.0	0.517	
	30	11.0	21.7	14.8	6.3	0.530	8.4	23.2	16.6	8.0	0.518	
	40	10.7	21.8	14.8	6.3	0.530	8.1	23.2	16.7	8.0	0.519	
	50	10.6	21.8	14.8	6.3	0.530	8.0	23.1	16.7	8.0	0.519	
	60	10.5	21.9	14.8	6.3	0.530	8.0	23.1	16.7	8.1	0.518	
	70	10.5	21.9	14.8	6.3	0.529	8.0	23.1	16.7	8.1	0.517	
	80	10.6	21.8	14.8	6.3	0.530	8.0	23.0	16.7	8.0	0.519	
	90	10.6	21.8	14.8	6.3	0.529	8.0	23.1	16.7	7.9	0.520	
	100	10.5	21.8	14.8	6.3	0.529	8.0	23.1	16.7	8.0	0.519	
Observed		10.9	8.1	12.8	9.0	0.56	9.1	18.5	16.7	7.0	0.56	

pressure, precipitation, and evaporation are taken from Schutz and Gates (1971, 1972) and that for wind speed and energy transfer from Oort and Rasmusson (1971). Figures 3, 4, and 5 show for each month the computed and observed fields of sea-level temperature, sea-level pressure, and precipitation. The latitudinal variation of the zonally-averaged values of each of the variables is shown in Figures 6 and 7.

Only the salient features of each figure will be described here.

(a) January sea-level temperature (Figs. 3a, 6a) - As mentioned earlier the computed values are generally too high in the polar regions, especially in January near the North Pole. As a result, the baroclinicity of the temperature field between 60 and 70°N is much weaker than observed, especially in the North Atlantic and North Pacific Oceans. This is partly due to the assumption of a constant lapse rate, but also to an inadequate reproduction of the warm ocean currents. Model temperatures in the eastern North Atlantic and Arctic Ocean are between 10 and 15°C lower than observed. These results suggest that on the scale of Figs. 3 to 5 the model dynamics and thermodynamics of the atmosphere and oceans need to be improved. In the tropics and in the southern hemisphere the model does fairly well.

(b) July sea-level temperature (Figs. 3b, 6b) - Again the

zone of strongest baroclinicity, along the coast of Antarctica, is not adequately reproduced by the model. Elsewhere, the results are not too bad, although parts of the tropics and subtropics are cooler than they should be. The major regions of upwelling and cool surface temperatures off the continental west coasts in the sub-tropics are only weakly reproduced by the model.

(c) January sea-level pressure (Figs. 4a, 6a) - The pressure field is coupled directly to the temperature field through (10) and (11). In spite of the simple parameterization, there is generally good agreement between observed and computed patterns. The major discrepancies are that in the model the Aleutian low pressure area is too far north (this shows up also in the zonally-averaged pressure distribution in Fig. 6a, in which the major northern hemisphere belts of low and high pressure are about 10° north of where they should be) and the southern hemisphere subtropical highs are too weak.

(d) July sea-level pressure (Figs. 4b, 6b) - Here the errors are larger than in January. Most obviously, the thermal lows over the northern hemisphere continents are much too far north (although the isobar configuration along the southern Asiatic coast is nearly correct). The subtropical highs of the northern hemisphere are too weak and also displaced north of where they should be, especially in the North Atlantic Ocean.

In the southern hemisphere the subarctic low is a bit too intense, but otherwise the computed pattern reproduces the observed fairly well.

(e) January precipitation (Figs. 5a, 6a) - The approach used in the model to determine precipitation was only moderately successful. There are some similarities between observed and computed patterns, but there are also major differences. Rainfall in parts of the tropics is badly overestimated (although for the entire tropical belt it is underestimated). Australia instead of being semi-arid is a center of heavy precipitation. This error may be traced to the coarse grid size used. The excessive precipitation in certain parts of the tropics may be due simply to an overestimate of the precipitable water vapor in the atmosphere in these latitudes. This quantity, in centimeters, is given by the denominator in (6). For a surface temperature of 30°C and a relative humidity of 80%, $e_0 = 33.94 \text{ hPa}$ and the precipitable water vapor equals 5.37 cm, which seems to be 15 to 30 percent higher than observed (Tuller, 1968).

Precipitation is grossly underestimated at latitudes between 30 and 60 N. As will be seen later, this is due to underestimates of both evaporation rates and the poleward transport of water vapor in the atmosphere (and its convergence). On the positive side, the precipitation maximum extending northeastward across the North Atlantic and associated with the middle-latitude storm

track is reproduced by the model.

(f) July precipitation (Figs. 5b, 6b) - Tropical precipitation is again overestimated, although the centers of maximum amounts are in approximately the correct locations. The monsoon rains of southeast Asia and India show up dramatically in the model. Computed precipitation amounts are also too high in subtropical and lower middle latitudes of the northern hemisphere. However, the relative distribution over the United States, with greatest amounts in the Southeast, is not unrealistic. The extreme aridity of the Sahara-Arabian desert area does not show up in the precipitation data. Nevertheless, in both January and July, this is the region where the model gives the lowest soil moisture content (15 to 25 percent of field capacity), the lowest relative humidities (15 to 20 percent) and the least cloud cover (0.08 to 0.12). The highest relative humidities (approaching 100 percent) and the greatest cloud cover (approaching 1.0) tend to occur near the winter pole.

(g) January evaporation (Fig. 6a) - The model does a poor job of reproducing the observed (or, rather, estimated) latitudinal distribution of evaporation. Especially noticeable are the gross underestimates poleward of 20° in the northern hemisphere and in the subtropics of the southern hemisphere. At first thought, this is hard to understand, since the equation used in the model to estimate evaporation from the oceans is basically the same as

that used to determine the observed values. What is different, however, is the air humidity. Although, through (19), an attempt is made to account for the advection of drier or more moist air from upwind, in (20) it is essentially assumed that the water and air are at the same temperature. This is certainly not the case in winter when cold, dry air frequently flows off the continents over warm ocean currents producing exceptionally high evaporation rates. Any further experiments with the model should correct for this. Here is where atmospheric dynamics are especially important.

(h) July evaporation (Fig. 6b) - Observed and computed evaporation rates do not agree much better in July than they do in January. This time the values are too high in middle latitudes of the northern hemisphere. Because of the way the model operates, an improvement in the estimates of evaporation should be accompanied by an improvement in estimates of precipitation.

(i) January wind velocity (Fig. 6a) - The computed zonal component of the velocity differs from the observed in two important respects. The northern hemisphere westerlies are too far north and the trade winds of the same hemisphere advance far enough southward across the equator to produce a belt of low-latitude westerlies in the southern hemisphere. Similarly for the meridional component, the Ferrel and Hadley cells of the northern hemisphere are, respectively, too far north and too intense.

(j) July wind velocity (Fig. 6b) - As in January, the northern hemisphere westerlies are too far north and a belt of westerlies appears near the equator, this time in the northern hemisphere and associated with an overly intense southern hemisphere Hadley circulation. Both the southern hemisphere westerlies and Ferrel cell are apparently too intense.

(k) January energy transport (Fig. 7a) - In Fig. 7 are shown the zonally-averaged north-south sensible heat (H), potential energy (P), latent heat (V) and total energy ($H+P+V$) transport in the atmosphere and the sensible heat transport (F) in the oceans for (a) January and (b) July. Negative values indicate a southward transport. Observed values, from Oort and Rasmusson (1971), are available only north of 10S and only for H , P , and V . In January, model and observed energy transport by the northern hemisphere Hadley circulation are in good agreement. Transport by the Ferrel cell is too weak and too far north. Since the potential energy transport is usually directed opposite to the sensible and latent heat transports, the sum of the three agrees reasonably well with that observed. The underestimate of the latent heat transport in middle latitudes of the northern hemisphere ultimately affects the precipitation rates obtained and should be corrected. The model yields a strong Ferrel cell transport in the southern hemisphere and a predominantly northward transport of heat by ocean currents.

(1) July energy transport (Fig. 7b) - Observed and computed curves agree fairly well except in the region affected by the northern hemisphere Hadley cell, the intensity of which is underestimated by the model. In July the model ocean transports heat primarily southward.

4. Conclusions

In this paper has been described what might be called a quasi-complete energy balance climate model, since the number of specified variables is almost minimal. These include only the solar radiation at the top of the atmosphere and the amounts of carbon dioxide and ozone in an atmospheric column. In addition, constraints are placed on several of the variables. For example, the temperature and vapor pressure lapse rates are given, the variation with height (or depth) of the northward velocity component is specified so that its vertically-averaged value is zero, and the sea-level pressure gradient is a unique function of the sea-level temperature gradient. Also, a few purely empirical (and speculative) relationships, such as (41) relating cloud cover to precipitation, potential evapotranspiration (or temperature), and relative humidity, are used.

Even with these (and other) relatively crude approximations, the model does surprisingly well in reproducing the observed climate (although it may be argued that it is constrained to do so).

The results are encouraging enough to warrant both further development of the model and its application to a number of interesting problems, including studies of the climatic effects of variations in the earth's orbit around the sun and of continental drift.

The model does not show the year-to-year variability of the actual climate, but settles down to a climate that is the same within each grid box from one year to the next. This may mean either that climatic change is due mainly to variations in external parameters, principally solar radiation and atmospheric aerosols, or, probably more likely, that the model either does not include or includes inadequately those processes primarily responsible for climatic variability. Certainly the linkage between the sea-level temperature field and all the other variables is not as strong in nature as it is in the model. Until this problem is resolved there is not much hope that the model could be used for climate predictability.

Based on the few experiments conducted so far, the model is probably intransitive for a wide range of initial conditions. It is likely, however, that a more extensive analysis will reveal that it behaves in the same manner as much simpler climate models. That is, for the present values of the external variables, primarily the solar constant, there may exist two additional solutions, one an ice-covered earth and the other a severe ice age type climate with global average temperatures 30 to 40 K colder than the present.

North (1975) shows that the latter is unstable under small perturbations away from equilibrium and, therefore, apparently of no physical significance. Sellers (1975) shows that the existence of this solution depends on how atmospheric processes, notably the absorption of solar radiation, are parameterized in the model.

It is hoped that there will be a place for this effort in the hierarchy of climate modeling. Admittedly it lacks the sophistication and scientific rigor of the joint ocean-atmosphere general circulation models. Nevertheless, it is better-suited than the bigger models to tackle the problem at hand, that of studying long-range climate change. Perhaps a merging of the two efforts would produce the most satisfying results. There are already certain similarities, for example in the way the hydrologic cycle is handled. The biggest differences are in the dynamics, treated elaborately in one and sketchily in the other. Admittedly it is aesthetically difficult to back off and simplify a physical system that has taken years to understand and to perfect, but this may be necessary if the best possible truly climatic model is to evolve.

Acknowledgments.

This research was supported by the Advanced Research Projects Agency of the Department of Defense and was monitored by the Air Force Office of Scientific Research under Contract No. AFOSR-74-2633. The author is grateful to Dick Sato and the National Center of Atmospheric Research for programming assistance and the use of the NCAR CDC 7600 computer and to Catherine Van Arnam of the Institute of Atmospheric Physics for typing the manuscript.

REFERENCES

- Adem, J., 1970: On the prediction of mean monthly ocean temperatures. Mon. Wea. Rev., 103, 410-430.
- Brooks, C. E. P., 1927: The mean cloudiness over the Earth. Mem. Roy. Meteor. Soc., 1, 127-138.
- Budyko, M. I., 1974: Climate and Life. Academic Press, 508 pp.
- Dietrich, G., 1963: General Oceanography, John Wiley & Sons, Inc., 588 pp.
- Fletcher, J. O., 1966: Proceedings of the symposium on the Arctic heat budget and atmospheric circulation. Memorandum RM-5233-NSF, The Rand Corporation, Santa Monica, 567 pp.
- Gordon, A. L., and H. W. Taylor, 1975: Seasonal change of Antarctic sea ice cover. Science, 187, 346-347.
- Haney, R. L., 1974: A numerical study of the response of an idealized ocean to large-scale surface heat and momentum flux. J. Phys. Oceanogr., 4, 145-167.
- McIlroy, I. C., and D. E. Angus, 1964: Grass, water, and soil evaporation at Aspendale. Agri. Meteor., 1, 201-224.
- Neumann, G., and W. J. Pierson, Jr., 1966: Principles of Physical Oceanography. Prentice-Hall, Inc., 545 pp.
- North, G. R., 1975: Analytical solution to a simple climate model with diffusive heat transport. J. Atmos. Sci. (to be published).
- Oort, A. H., and E. M. Rasmusson, 1971: Atmospheric circulation statistics, NOAA Professional Paper 5, 323 pp.

Schutz, C., and W. L. Gates, 1971: Global climatic data for surface, 800 mb, 400 mb: January. R-915-ARPA, The Rand Corporation, Santa Monica, 173 pp.

_____, and _____, 1972: Global climatic data for surface, 800 mb, 400 mb: July. R-1029-ARPA, The Rand Corporation, Santa Monica, 180 pp.

Sellers, W. D., 1965: Physical Climatology, Univ. of Chicago Press, 272 pp.

_____, 1973: A new global climatic model. J. Appl. Meteor., 12, 241-254.

_____, 1974: A reassessment of the effect of CO₂ variations on a simple global climatic model. J. Appl. Meteor., 13, 881-833.

_____, 1975: Climate models and variations in the solar constant. Geofisica Internacional (to be published).

Tuller, S. E., 1968: World distribution of mean monthly and annual precipitable water. Mon. Wea. Rev., 96, 785-797.

Vowinckel, E., and S. Orvig, 1970: The climate of the north polar basin. World Survey of Climatology, 14, 129-252.

Figure legends

Fig. 1. Flow diagram for the climate model. NC and C represent, respectively, non-convergent and convergent paths. The variables computed in each of the numbered blocks are listed in the text. The index i refers to longitude and ranges from 1 to 36.

Fig. 2. The solid lines give the time variation of the sea ice area (the average of the July and January values) for the northern (N and N1) and southern (S and S1) hemispheres. N and S are for a solar constant of 1360 Wm^{-2} ; N1 and S1 are for a solar constant of 1353 Wm^{-2} . To test the stability of the model ice and snow cover, the high solar constant case was rerun for 10 years with initial conditions of (a) no ice or snow anywhere (dashed lines) and (b) no ice or snow and temperatures everywhere above 274K (dash-dotted lines).

Fig. 3a. The average sea-level temperature field ($^{\circ}\text{C}$) in January, (a) given by the model after a computer run of 100 model years (top) and (b) observed (bottom, after Schutz and Gates, 1971).

Fig. 3b. The same as Fig. 3a, except for July. The observed field is from Schutz and Gates (1972).

Fig. 4a. The average sea-level pressure field (hPa-1000) in January (a) given by the model after a computer run of 100 model years (top) and (b) observed (bottom, after Schutz and Gates, 1971).

Fig. 4b. The same as Fig. 4a, except for July. The observed field is from Schutz and Gates (1972).

Fig. 5a. The average precipitation field (cm mo^{-1}) (a) given by the model in January after a computer run of 100 model years (top) and (b) observed for December through February (bottom, after Schutz and Gates, 1971).

Fig. 5b. The same as Fig. 5a, except for July. The observed field, averaged for June through August, is from Schutz and Gates (1972).

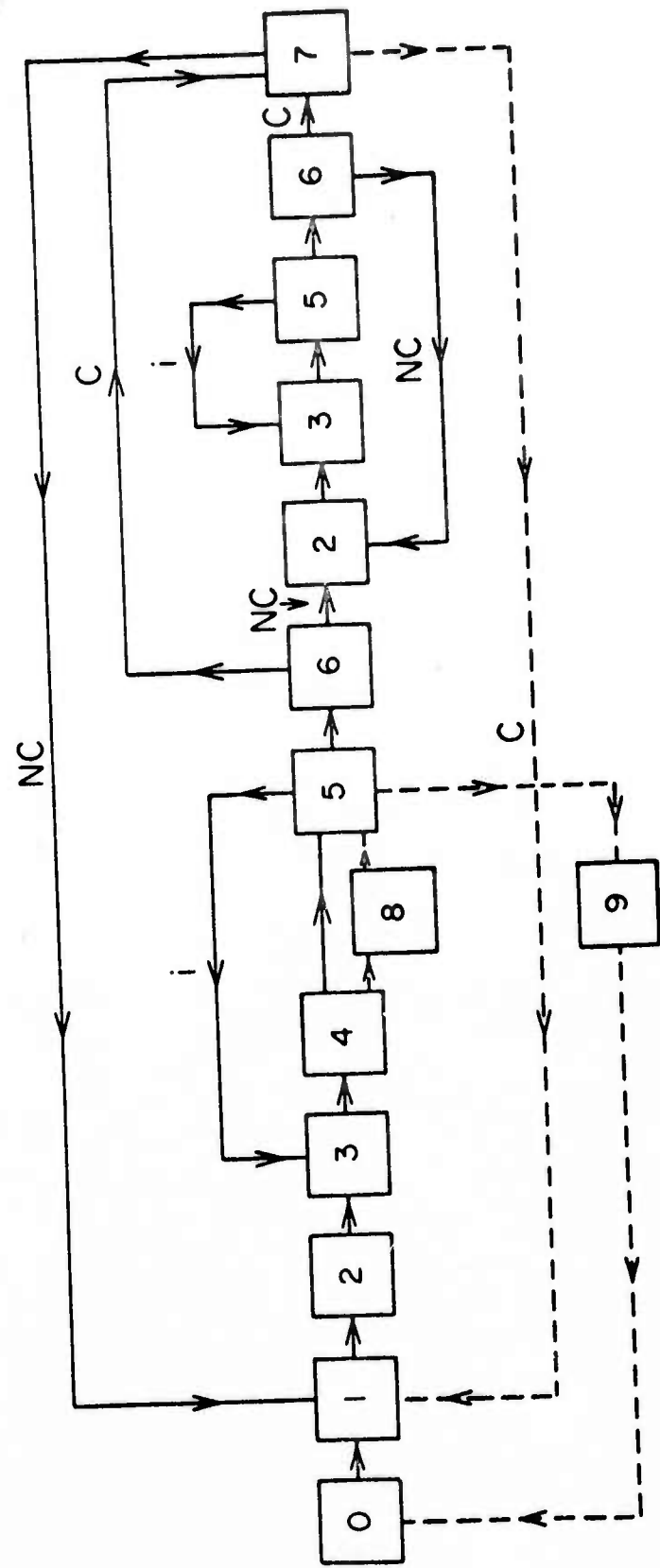
Fig. 6a. The latitudinal distribution of the computed (solid lines) and observed (dashed lines) zonally-averaged values of sea-level temperature T_o ($^{\circ}\text{C}$), sea-level pressure p_o (hPa), precipitation $r(\text{cm mo}^{-1})$, evaporation $E(\text{cm mo}^{-1})$, zonal wind speed $u(\text{m sec}^{-1})$, and meridional wind speed $v(\text{m sec}^{-1})$, zonal wind speed $u(\text{m sec}^{-1})$, and meridional wind speed $v(\text{m sec}^{-1})$ in January. Winds from the west and from the south are positive. The computed values are those obtained from a model run of 100 years. The observed values of T_o , p_o , r and E are from Schutz and Gates (1971). r and E are averages for December through February. The observed values of u and v are from Oort and Rasmusson (1971).

Fig. 6b. The same as Fig. 6a, except for July. The observed values of T_o , p_o , r and E are from Schutz and Gates (1972); r and E are averages for June through August.

Fig. 7a. The latitudinal distribution of the computed (solid lines) and observed (dashed lines) zonally-averaged values of the meridional transport ($10^{21} \text{ J mo}^{-1}$) of sensible heat H , potential energy P , latent heat V , atmospheric energy $H+P+V$, and sensible heat by ocean currents F . Note that expanded ordinates are used for the latter three. Negative values indicate a southward transport. The computed values are those obtained from a model run of 100 years. The observed values are from Oort and Rasmusson (1971).

Fig. 7b. The same as Fig. 7a, except for July.

FIGURE 1



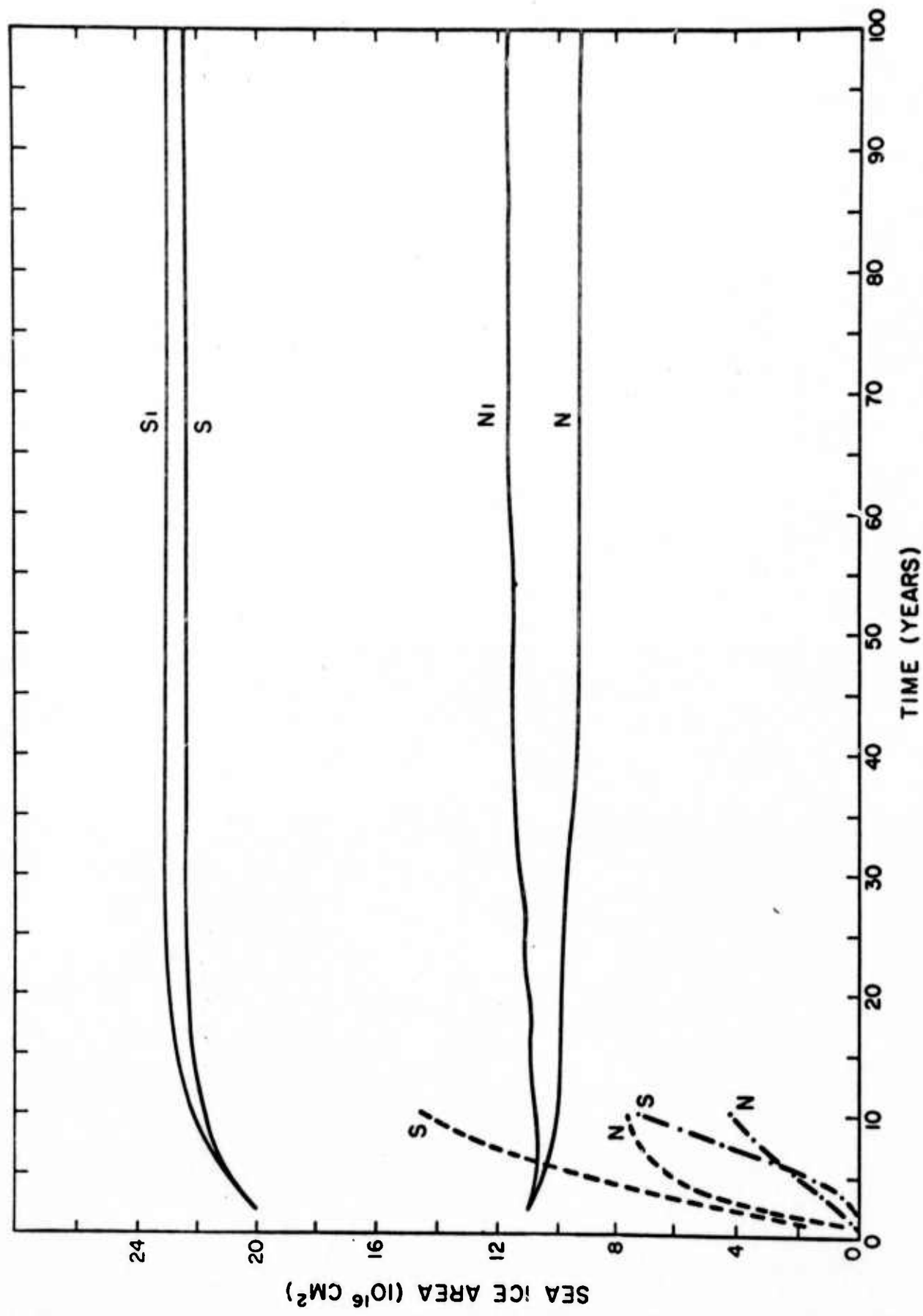


FIGURE 2

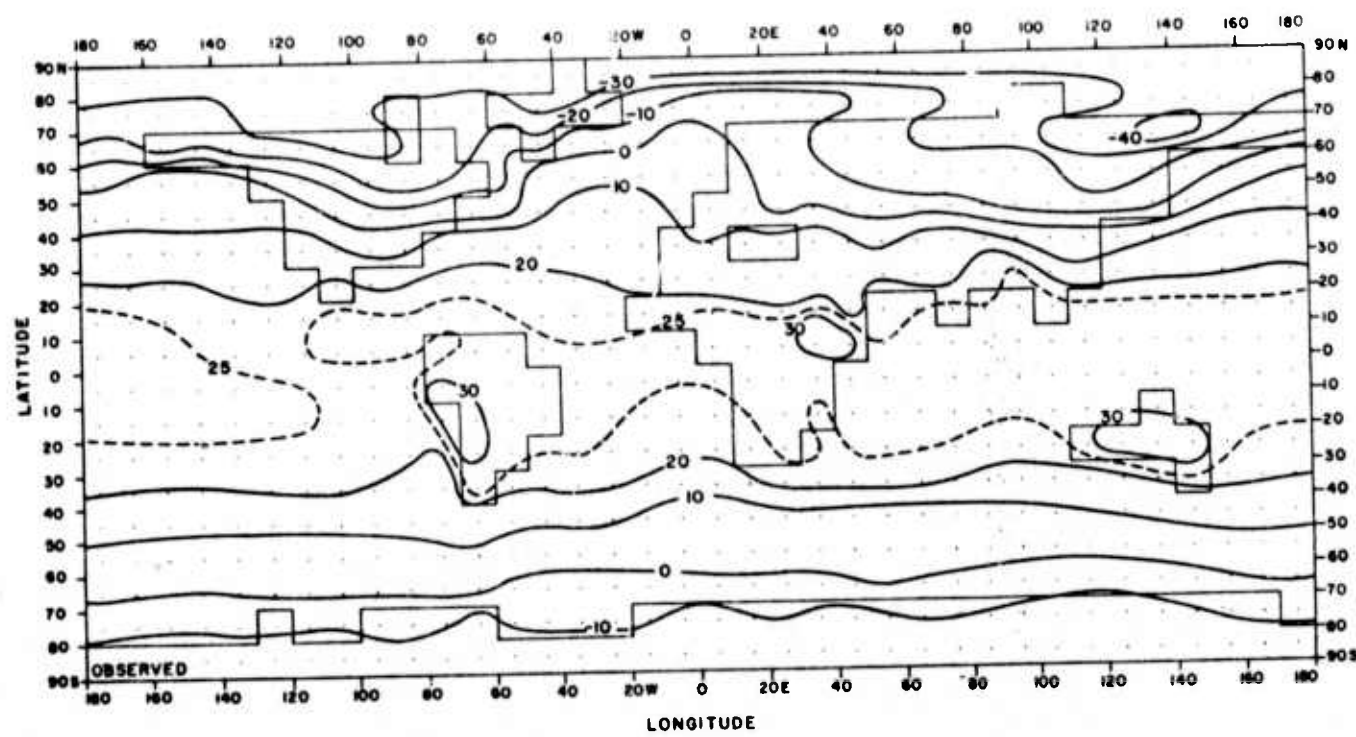
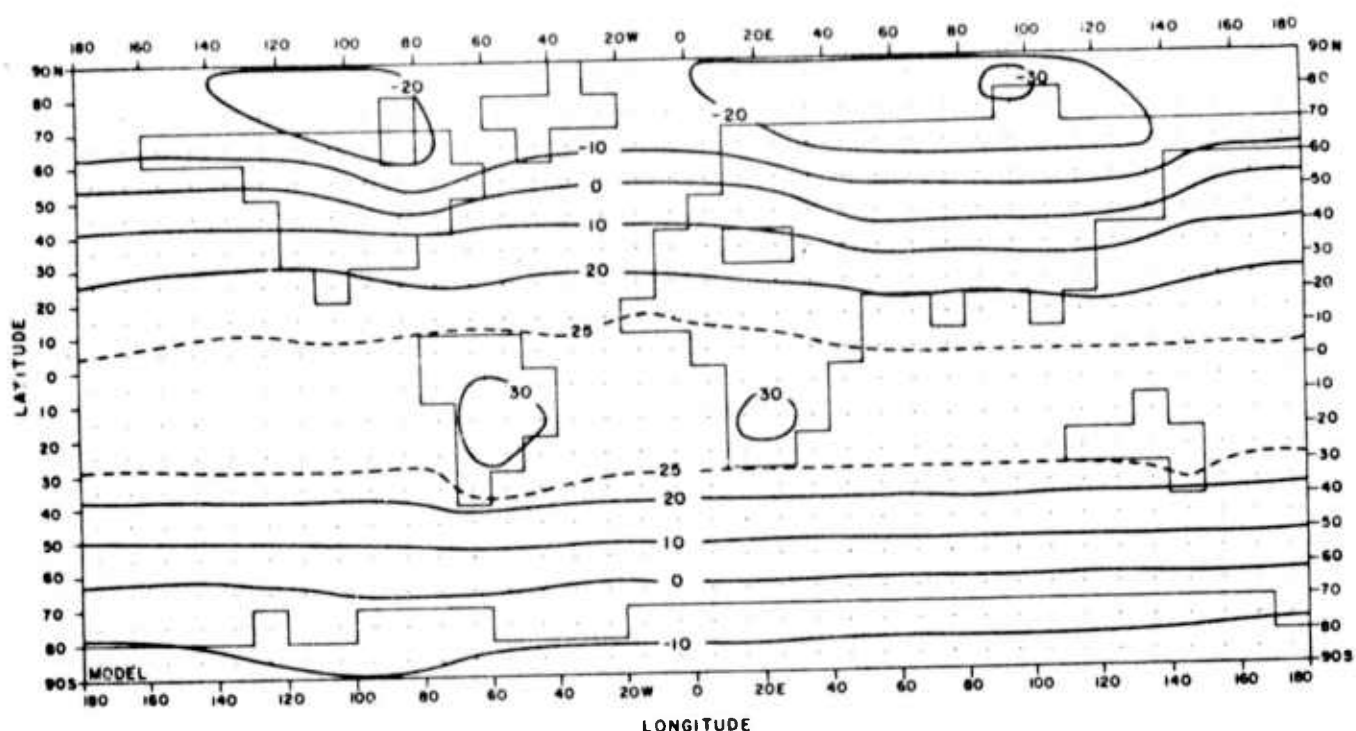


FIGURE 3a-

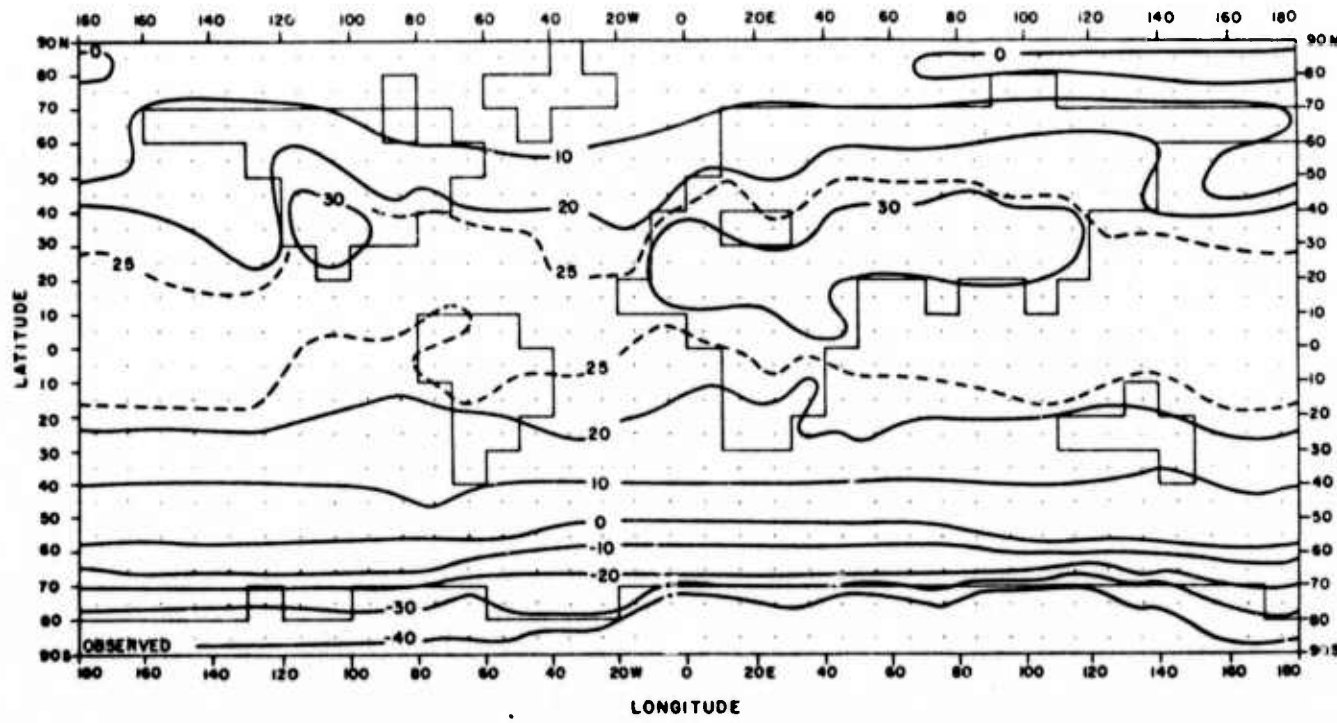
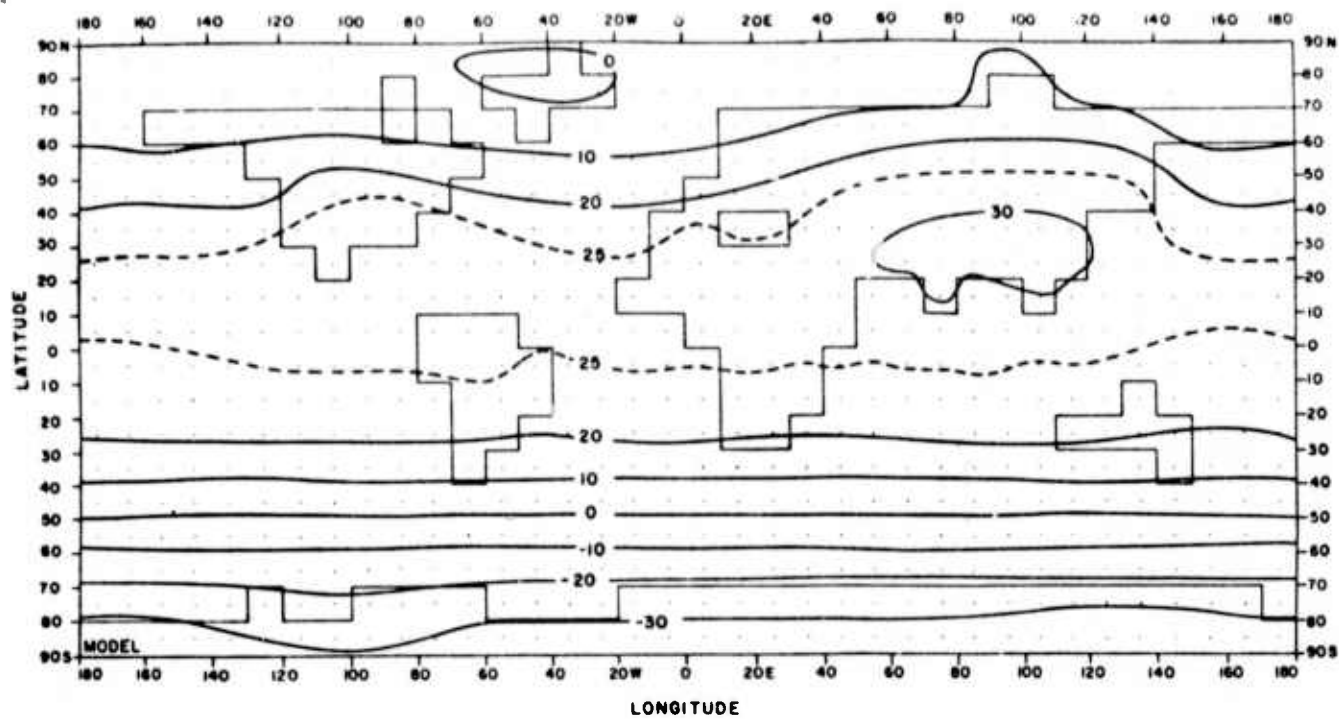


FIGURE 3.8

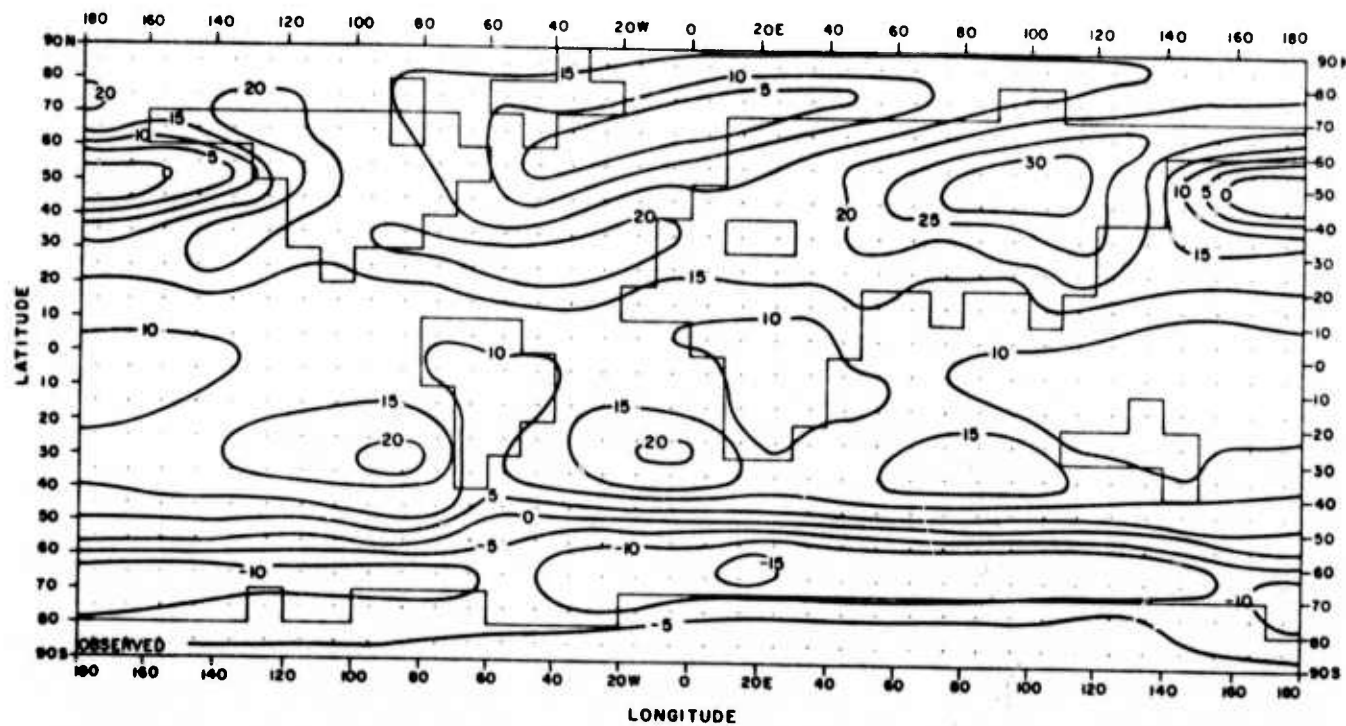
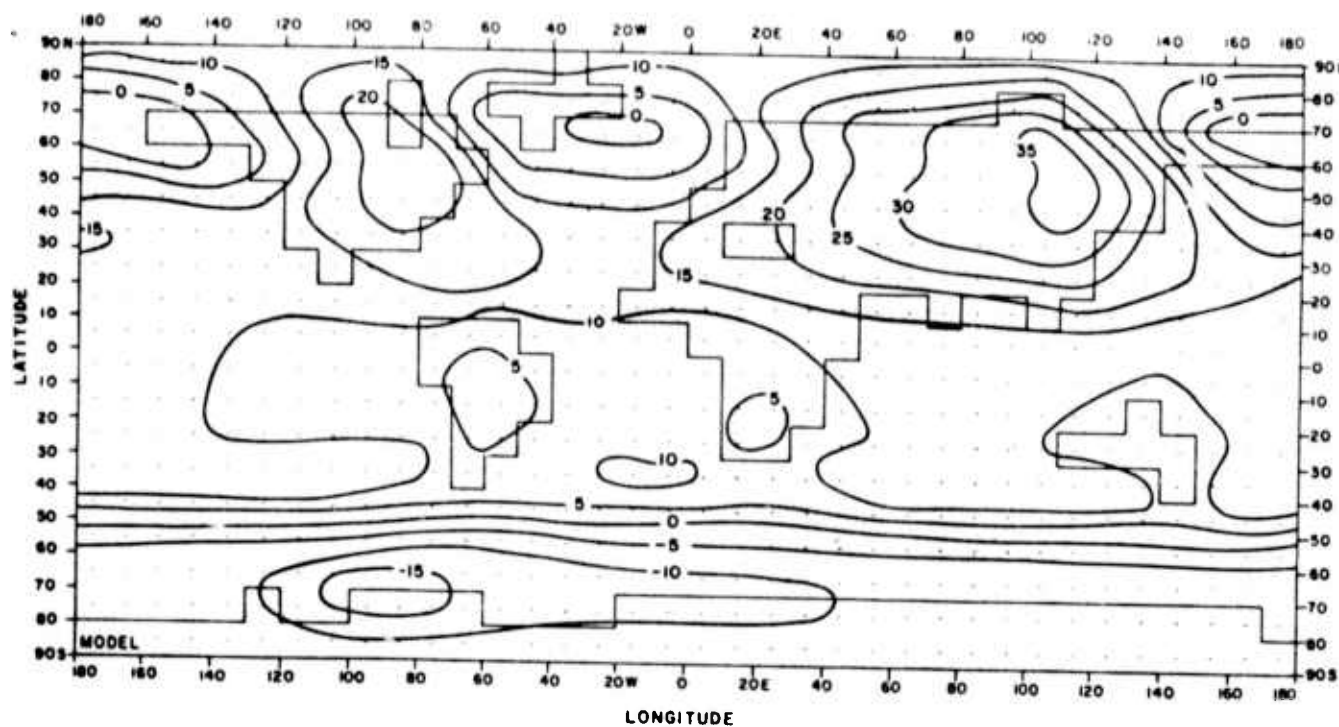


FIGURE 4a

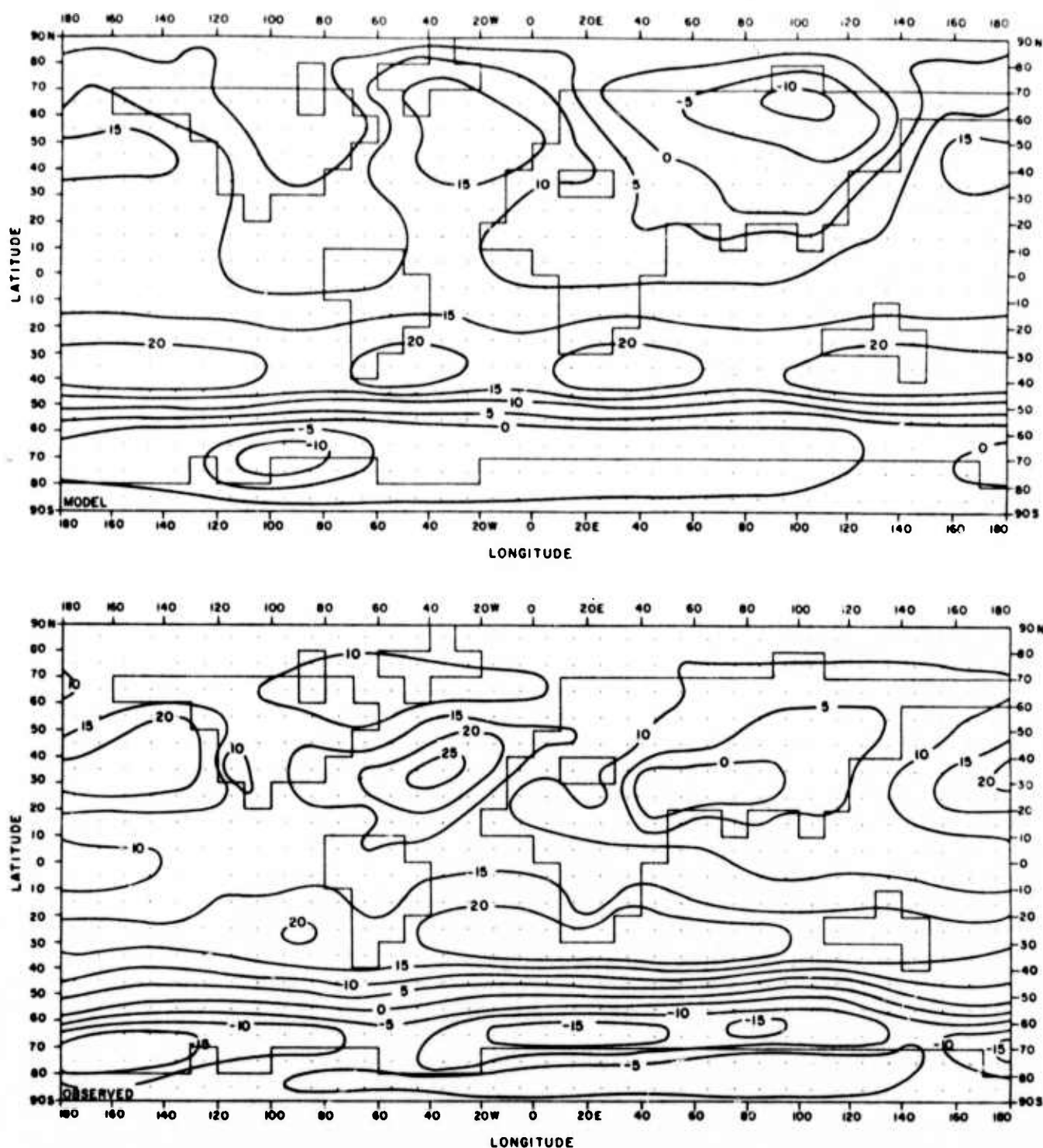


FIGURE 4-8

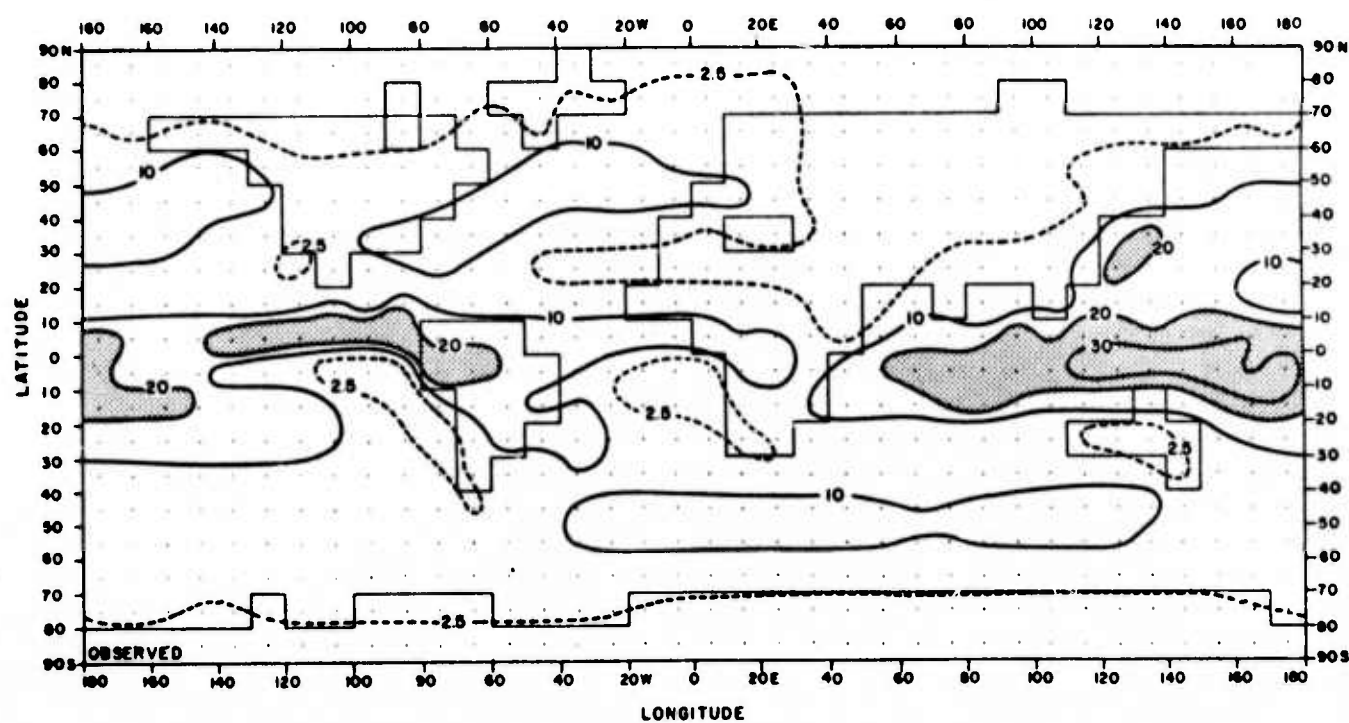
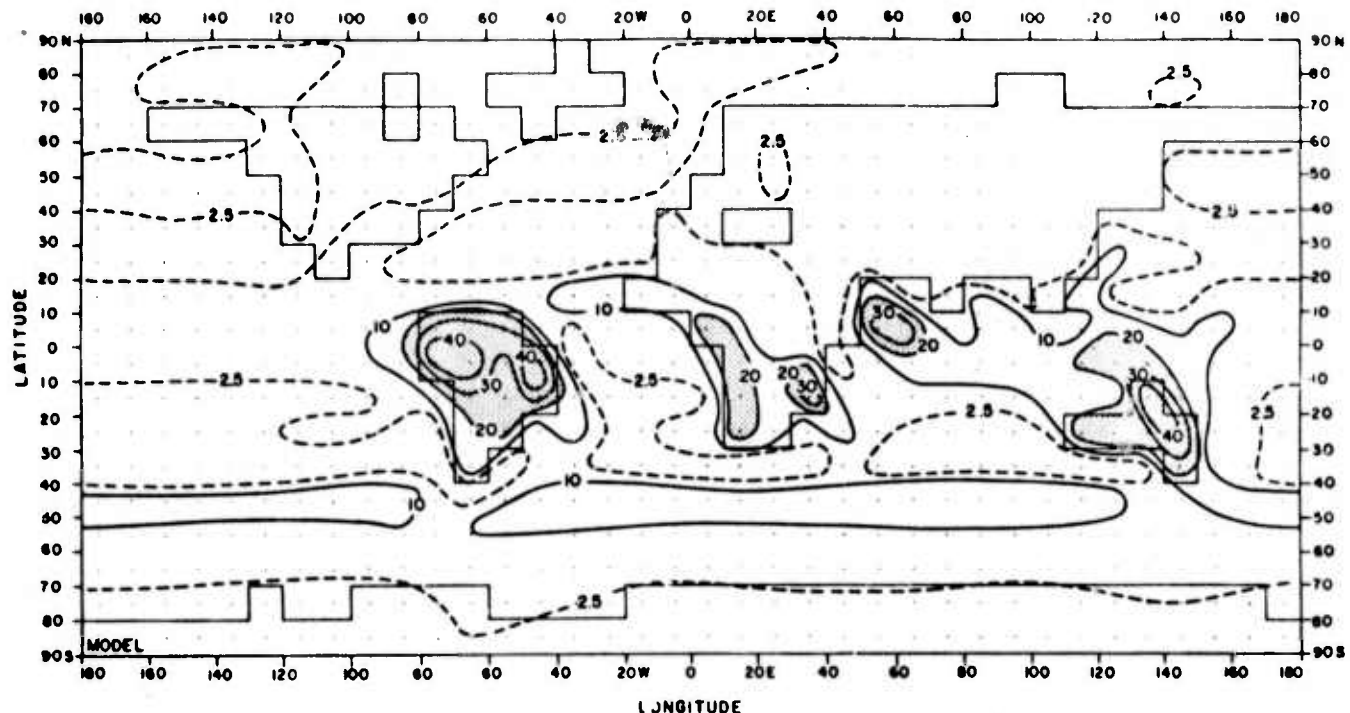


FIGURE 5a

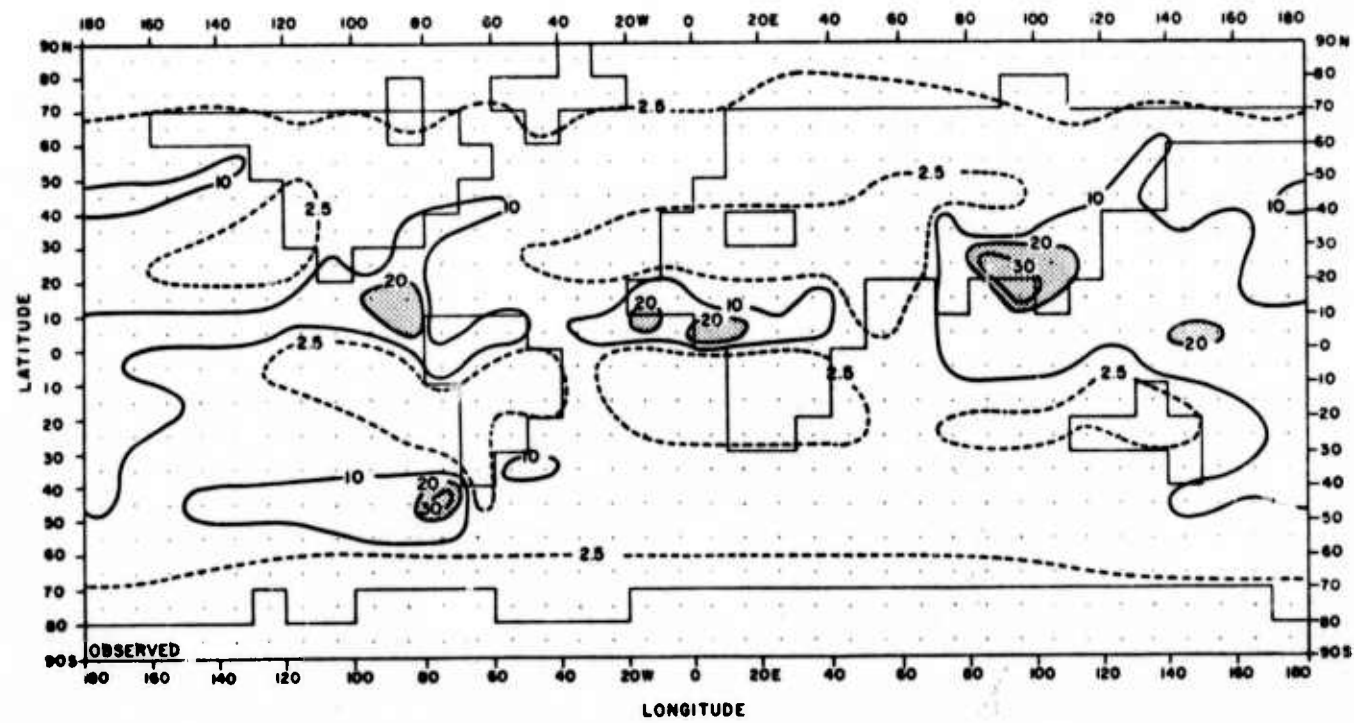
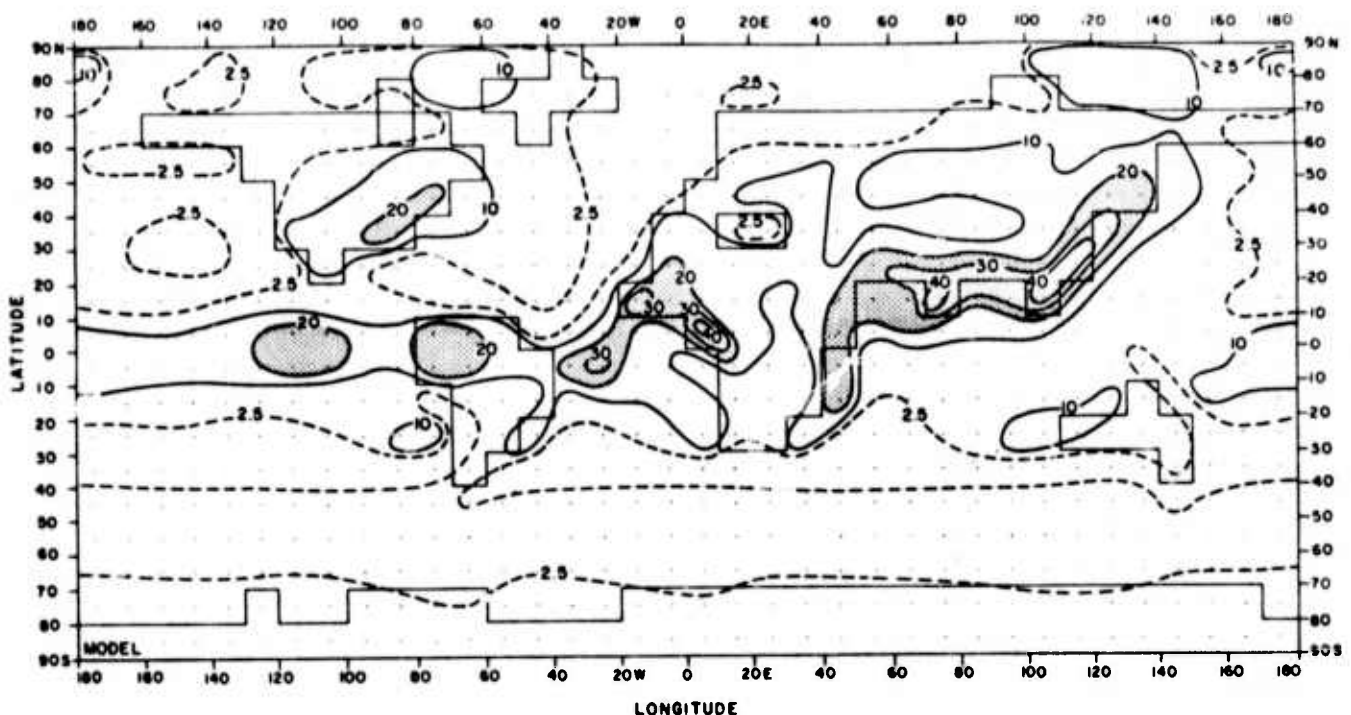


FIGURE 5c

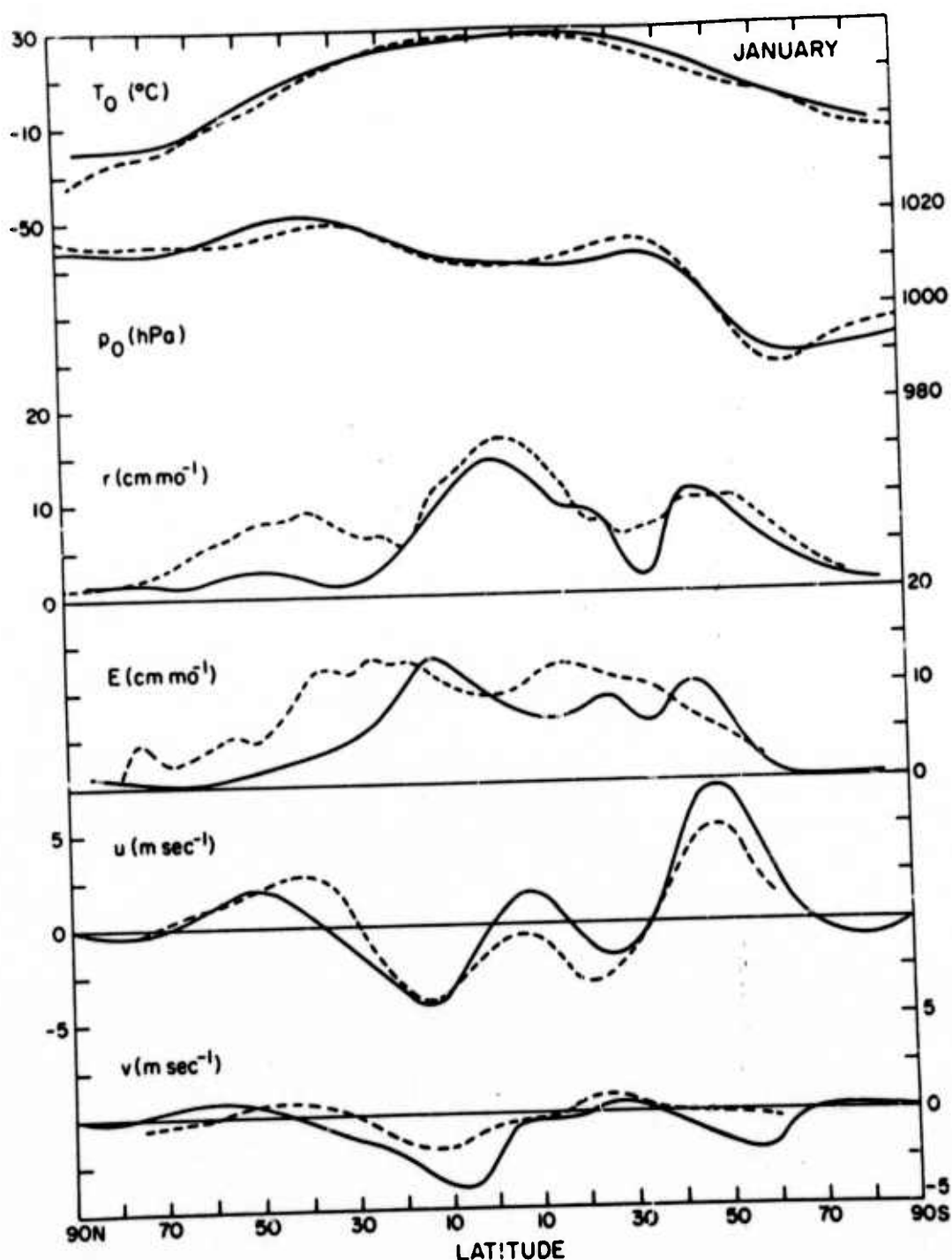


FIGURE 6a

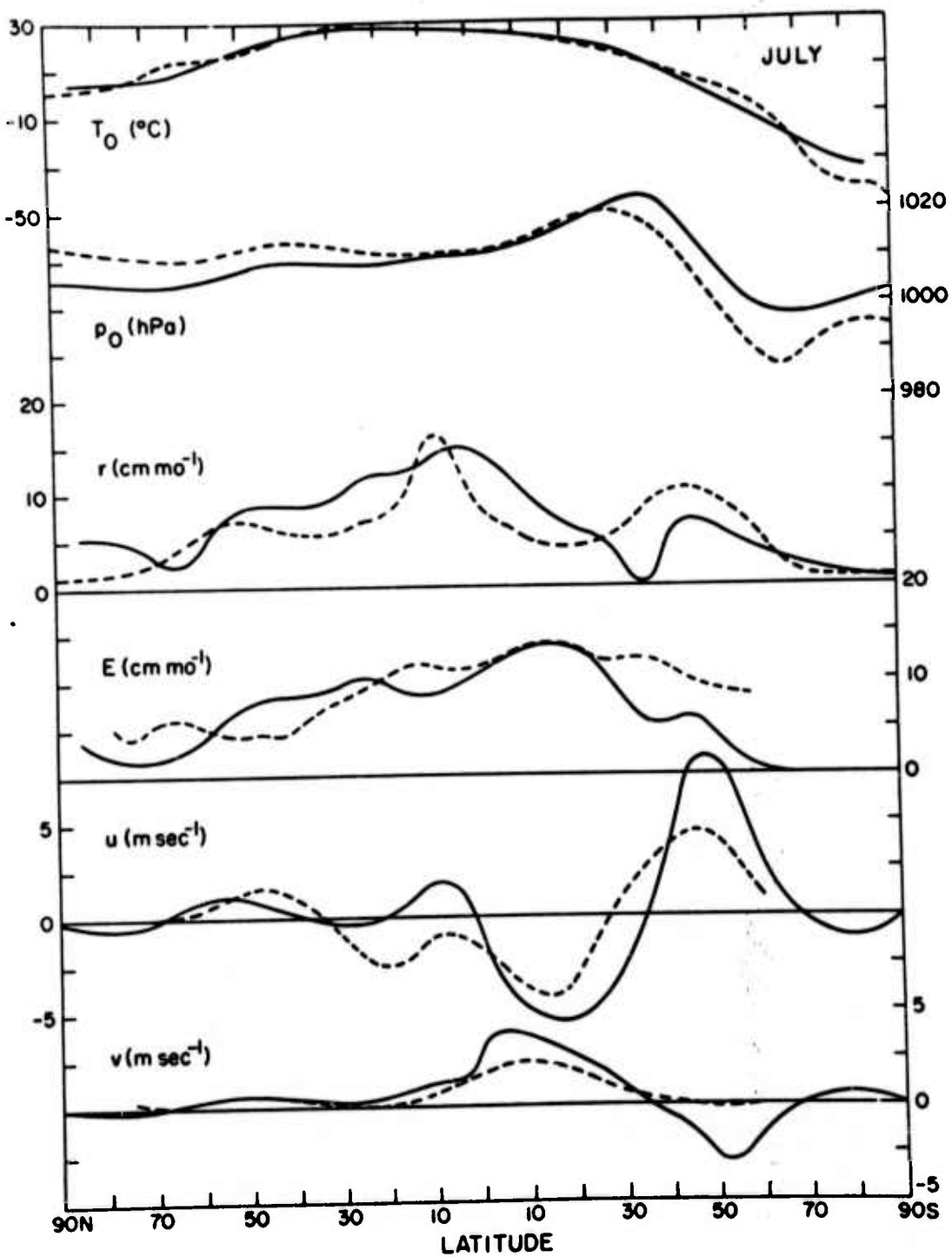


FIGURE 6.R

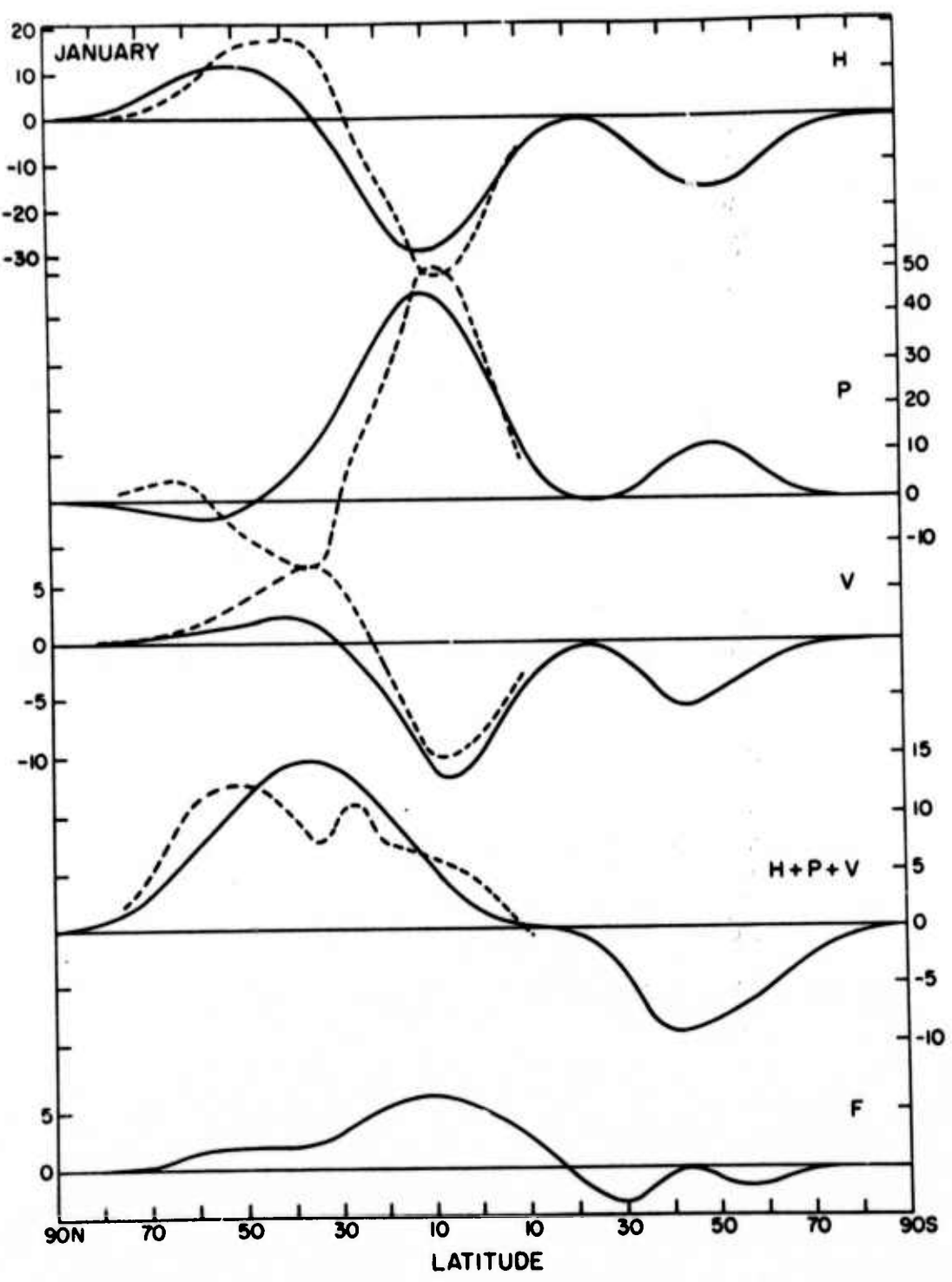


FIGURE 7a

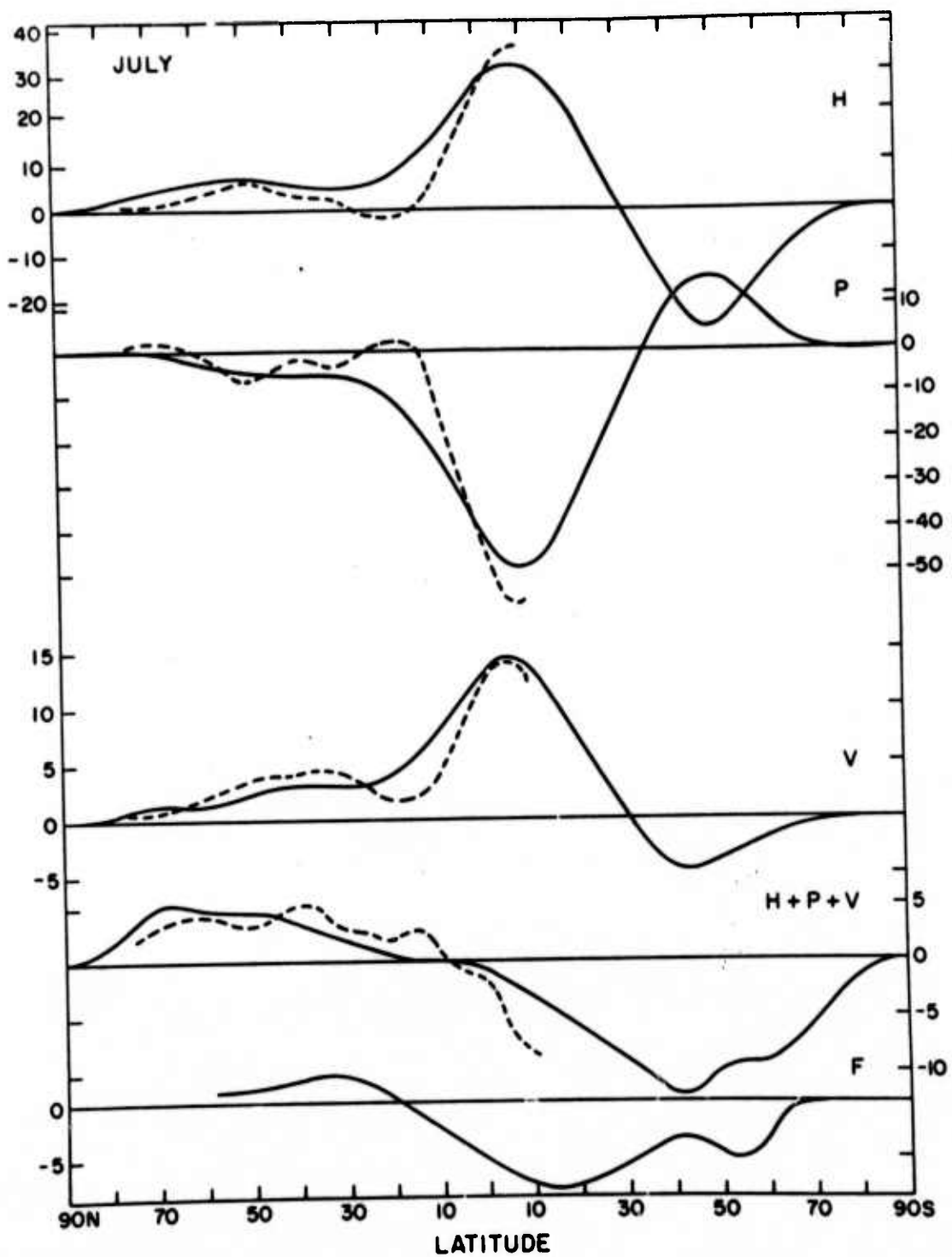


FIGURE 7.8